Annals of Biomedical Engineering
https://doi.org/10.1007/s10439-026-04057-1

BMES BIOMEDICAL ENGINEERING SOCIETY

ORIGINAL ARTICLE

Biomechanically Informed Patient-Specific in Silico Models for Laser Refractive Surgery

Benedetta Fantaci[1] · Elena Redaelli[1,2] · Mònica Martí[3] · Gemma Julio[3] · Anton Barraquer[3] · Jose Lamarca[3] · Jorge Grasa[1,4] · Begoña Calvo[1,4]

Received: 23 October 2025 / Accepted: 22 February 2026

Abstract

Purpose: Corneal biomechanics plays a key role in the planning and outcomes of laser refractive surgery. This study presents a validated methodology for simulating patient-specific refractive treatments, focusing on the optomechanical effects of the three most commonly performed procedures: PRK, LASIK, and SMILE.

Methods: For the first time, patient-specific mechanical properties of the cornea were incorporated into finite element simulations. These properties were estimated using an artificial neural network trained on *in silico* data from fluid–structure interaction models of non-contact tonometry. The tool takes as input corneal deformation images acquired with the Corvis ST device, intraocular pressure (IOP), and corneal geometry obtained from Pentacam imaging. IOP is estimated independently of corneal geometry and mechanical properties using a novel algorithm developed in prior studies. The methodology was tested on a cohort of 58 eyes from 29 patients who underwent one of the three procedures.

Results: By integrating patient-specific geometry, IOP, and biomechanical characterization, the proposed framework successfully simulated postoperative corneal responses, yielding a mean dioptric error of $+0.40 \pm 0.30$ D relative to clinical outcomes. Among the three procedures, SMILE produced the highest mechanical impact on the corneal model.

Conclusion: This study introduces a personalized, biomechanically informed approach to simulate corneal behavior following refractive surgery. The proposed framework enhances surgical planning and improves prediction of postoperative refractive stability, offering a step toward personalized refractive correction and safer, more predictable clinical outcomes.

Keywords Corneal behavior · Refractive surgery · Finite element method · Corneal mechanical properties · Artificial neural network · Non-contact tonometry

Introduction

Recently, the role of corneal biomechanics in the pre-surgical planning and outcome of laser refractive treatments has raised growing interest among clinicians and scientists [1]. Laser refractive procedures alter corneal biomechanics by reshaping corneal geometry to achieve the dioptric correction target. Consequently, the cornea reaches a new biomechanical equilibrium that depends on the tissue's mechanical properties and the action of intraocular pressure (IOP) within the eye.

Three main procedures are performed in daily clinical practice [2]: Photorefractive Keratectomy (PRK), where the anterior limiting lamina (ALL) and the stroma are directly ablated with an excimer laser, after epithelial removal; Laser In-Situ Keratomileusis (LASIK), which involves creating a hinged flap with a femtosecond laser, lifting it to expose

Associate Editor Joel Stitzel oversaw the review of this article.

✉ Benedetta Fantaci
bfantaci@unizar.es

1 Aragón Institute of Engineering Research (I3A), Universidad de Zaragoza, Zaragoza, Calle de Mariano Esquillor Gómez s/n, 50018, Spain

2 Instituto de Óptica "Daza de Valdés", Consejo Superior de Investigaciones Científicas (IO-CSIC), Calle de Serrano, 121, Madrid 28006, Spain

3 Centro de Oftalmología Barraquer, Carrer de Muntaner, 314, Sarriá-Sant Gervasi, Barcelona 08021, Spain

4 Centro de Investigación Biomédica en Red en Bioingeniería, Biomateriales y Nanomedicina (CIBER-BBN), Avenida Monforte de Lemos, 3-5, Madrid 28029, Spain

and ablate the stroma with an excimer laser, while preserving the epithelium and the ALL; and Small Incision Lenticule Extraction (SMILE), where a femtosecond laser is used to create a lenticule in the corneal stroma, which is then extracted through a 2 mm incision, preserving the anterior cornea's integrity.

Assessing corneal biomechanics during a patient's pre-surgical evaluation is crucial to ensure an optimal outcome and avoid post-surgical complications (e.g, ectasia). On the other hand, the selection of the procedure should also be based on a thorough understanding of the biomechanical changes caused by each treatment, as they differ consistently, as it will be later demonstrated in this study. Corneal biomechanics is currently assessed in clinical practice using non-contact tonometers (NCT), such as Corvis ST (Oculus Optikgeräte GmbH, Wetzlar, Germany), which applies an air puff to the cornea and records its deformation with a high-speed camera [3]. The device estimates the IOP and computes several parameters to evaluate corneal tissue's response, determining patient's eligibility to undergo the procedure, including the evaluation of ectasia's risk. However, there is currently no clinical device that offers feedback to clinicians regarding the biomechanical impact of a chosen procedure or enables virtual testing of different surgical options on the patient to evaluate their biomechanical effects and predict the optical outcome.

On the other hand, once the surgeon has selected the procedure, the laser system does not account for the patient-specific mechanical response of the cornea to the refractive treatment, when determining the ablation depth. In other words, the treatment plan is not tailored to the individual biomechanical properties of the patient's cornea. For example, excimer lasers such as the Wavelight EX500 by Alcon (Fort Worth, Texas, USA) or femtosecond lasers like the VisuMax® by Zeiss (Oberkochen, Germany) establish the wavefront-optimized ablation profile solely based on the patient's refractive error, without requiring any biomechanical input. The final optical outcome strictly depends on the postoperative geometrical configuration of the cornea, which, in turn, is influenced by how the cornea deforms after ablation, whose behavior is determined by patient-specific biomechanical properties. As a result, residual refractive errors within ± 1 diopter often remain uncorrected [4], ultimately reducing surgical precision. Incorporating corneal biomechanics into the treatment planning can help overcome these limitations, leading to improved surgical outcomes and reducing the incidence of residual refractive errors.

Finite element (FE) models constitute a powerful tool to address this clinical limitation, as they incorporate the mechanical behavior of the system and can provide surgeons with biomechanical insights to support pre-surgical decision-making. To replicate the biomechanics of corneal tissue, these models require the mechanical properties of the corneal tissue as input and yield mechanical outputs such as displacements (closely related to the corneal dioptric power), stresses, and strains.

Indeed, computational modeling has been widely applied in the literature to investigate corneal biomechanical changes induced by laser refractive procedures [5–18]. In parallel to full 3D FE approaches, reduced-order formulations have been proposed to efficiently capture corneal deformation, e.g., a 2D generalized plate model with kinematically independent thickness applied to keratoconus and post-keratoplasty corneas, showing promising results in describing corneal shape changes in these conditions [19].

However, these studies relied on average material properties rather than patient-specific ones. While the use of average properties may be acceptable for qualitative assessment of the mechanical impact of refractive treatments, it becomes a significant limitation when the goal is pre-surgical planning and accurate outcome prediction. In such cases, accounting for patient-specific material properties is essential. This shortcoming compromises the optical accuracy of the models, which require micrometric precision to ensure reproducibility.

Artificial intelligence (AI) approaches have recently been employed together with in silico models to estimate the biomechanical properties of soft tissues. Nagle et al., [20] developed an artificial neural network (ANN) to predict patient-specific skin growth rate, shear modulus, and natural pre-stretch with a high level of accuracy. Ahamdi et al., [21] integrated FE analysis and physics-informed neural networks to predict material properties of the human lumbar spine. In a previous study by our group [22], we developed an ANN trained on in silico data generated from fluid–structure interaction (FSI) FE simulations replicating Corvis ST deformation behavior [23]. This ANN is capable of estimating the in vivo material properties of corneal tissue in real time, offering a non-invasive method for patient-specific biomechanical characterization. Once the material properties are estimated, they can be given as input to FE in silico models of refractive surgeries to incorporate the patient-specific biomechanical behavior of the cornea.

In this work, we present the application of the above-mentioned tool for real-time estimation of patient-specific corneal properties in a cohort of 58 eyes of 29 patients who underwent refractive surgery (PRK, LASIK, and SMILE), integrated into a detailed methodology for simulating laser refractive treatments. The overall approach is validated against Pentacam-derived keratometric outcomes (rotating Scheimpflug imaging), which provide a robust description of postoperative corneal shape changes [24].

Materials and Methods

Patients Enrollment and Pre-surgical Evaluation

Retrospective data of patients aged between 21 and 47 years with myopia or myopic astigmatism who underwent laser refractive surgery between 2020 and 2024 were collected. Both eyes of 29 patients with spherical error between −2.00 D and −5.00 D were included. Among them, ten underwent PRK, ten LASIK, and nine SMILE treatment.

Data were anonymized by our clinical partner, Centro de Oftalmología Barraquer (Barcelona, Spain). Data acquisition followed good clinical practices and adhered to the tenets of the Declaration of Helsinki. This study was approved by the Comité de Ética de la Investigación con medicamentos (CEIm) of Centro de Oftalmología Barraquer, Spain (CEIm code: 207_Modelización_Qx_Rx). Patients included in the study did not present any other ocular or systemic pathologies that could affect corneal biomechanics or refractive outcomes.

Each participant underwent a complete pre-surgical evaluation, including vision tests and ophthalmic exams, among which Pentacam HR (Oculus Optikgeräte GmbH, Wetzlar, Germany) topography and Dynamic Scheimpflug Analyzer Corvis ST (Oculus Optikgeräte GmbH, Wetzlar, Germany) exam were used for model construction and material properties definition (see Sect. 2.3). Clinical exams were repeated between 3 and 10 months after surgery, based on patient's availability.

Table 1 reports the descriptive statistics for the following parameters in the pre-surgical setting: age, pachymetry, Deflection Amplitude, biomechanically corrected Intraocular Pressure (bIOP), Stress–Strain Index (SSI), and the refractive surgery correction. For each parameter, the mean, standard deviation, minimum, maximum, and the 25th, 50th (median), and 75th percentiles are provided. Age refers to the age of the subjects at the time of surgery. Pachymetry (Pachy) represents the central corneal thickness (CCT) in μm, which is a key structural parameter that influences the biomechanical behavior of the cornea. Deflection Amplitude (Def. Amp.), measured in mm, indicates the maximum displacement of the corneal apex in response to the air puff. The bIOP is the biomechanically corrected intraocular pressure, expressed in mmHg, which is a corrected IOP value provided by Corvis ST. The Stress–Strain Index (SSI) is a dimensionless measure to qualitatively characterize corneal stiffness also provided by Corvis ST device. The spherical equivalent (SE) of a refractive error is the single-power lens that best approximates the focus of a sphero-cylindrical prescription, defined as $SE = Sphere + Cylinder/2$. These descriptive values offer an overview of the distribution and variability of each parameter in the studied population.

Surgical Techniques

PRK

Chemical corneal de-epithelialization was performed and epithelium was removed manually. Wavelight® EX500 excimer laser by Alcon (Forth Worth, Texas, USA) was used to perform PRK treatment. In all interventions, a 6.5-mm optical zone with 1.25 transition was applied for laser ablation. After the ablation, mitomycin was administrated and therapeutic contact lenses were applied.

LASIK

Femtosecond lasers Visumax® by Zeiss (Oberkochen, Germany) or Intralase® by Abbott (Chicago, Illinois, USA) were used for flap creation. Flap dimensions varied among the patients: flap diameter varied between 7.9 mm and 9 mm, flap thickness between 95 µm and 100 µm, and hinge was positioned at 90° and had a length between 3.45 mm and 3.89 mm (Table 3). Wavelight® EX500 excimer laser by Alcon (Forth Worth, Texas, USA) was used to perform PRK treatment. In all interventions, a 6.5 mm optical zone with 1.25 transition was applied for laser ablation.

Table 1 Patient data analysis

	mean ± std (min/max)	25%	50%	75%
Age [years]	33.55 ± 7.15 (21/47)	27.00	34.00	38.00
Pachy [μm]	546.36 ± 28.75 (492.00/612.00)	522.50	543.00	569.00
Def. Amp. [mm]	1.08 ± 0.10 (0.82/1.28)	1.03	1.09	1.15
bIOP [mmHg]	15.20 ± 1.86 (11.80/22.50)	14.15	14.75	16.00
SSI [-]	0.99 ± 0.17 (0.60/1.42)	0.89	0.97	1.06
Spherical Equivalent [D]	−3.65 ± 1.33 (−1.5/−6.25)	−4.75	−3.44	−2.63

For each variable the mean, standard deviation (std), minimum value (min), maximum value (max), and 25, 50, and 75 percentile are reported

SMILE

Femtosecond laser Visumax® by Zeiss (Oberkochen, Germany) was used for lenticule creation and incision. Cap dimensions varied among the patients: cap diameter varied between 7.5 mm and 7.6 mm, cap thickness between 120 µm and 160 µm, incision was performed at an angle between 110° and 135°, and had a length between 2 mm and 2.5 mm (Table 4). In all interventions, a 6.5-mm optical zone with 0.1 transition zone was considered for lenticule creation.

Topical postoperative medication protocols varied depending on the surgical technique. PRK patients were treated with topical antibiotics (Ofloxacin 3 mg/ml (Exocin®, Allergan Parmaceuticals Ireland), administered 5 times/day for one week or until complete reepithelialization of the cornea), analgesics (Sodium diclofenac 1 mg/ml (Diclofenaco-lepori, Tubilux Pharma), applied 3 times/day for three days), and corticosteroids (Dexamethasone phosphate 1 mg/ml (Dexafree®, Thea), prescribed 3 times/day for one week, starting after discontinuation of diclofenac, followed by Fluorometholone 1 mg/ml (FML®, Allergan Parmaceuticals Ireland) in a reducing posology: 3 times/day for one month, 2 times/day for the next month, and 1 time/day for the final month). Artificial tears (Systane® Ultra by Alcon or Hylo Comod® by Ursapharm or Hyabak® by Thea) were also prescribed, with intensive use (1 drop every hour) during the initial postoperative period and then 4 times/day for 2–6 months. If needed, patients could orally assume Metamizole magnesium (NOLOTIL®, Boehringer Ingelheim Spain), Ibuprofen, or any other analgesic. For LASIK and SMILE patients, a similar regimen was followed, including antibiotics and corticosteroids (Tobramycin 3 mg/ml and Dexamethasone 1 mg/ml (Tobradex®, Novartis Pharmaceutica), administered 3 times/day for one week) alongside artificial tears (1 drop every hour for the first week, then 4 times/day for 2–6 months).

Patient-Specific Material Properties and IOP

The estimation of the IOP in Corvis ST is based on the first applanation time of the cornea during the air jet, that is the time it takes for the cornea to flatten for the first time after an air puff is applied. The first applanation occurs when the inward movement of the cornea, induced by the air puff, reaches a point where the curvature of the corneal surface becomes flat. However, the accuracy of the IOP estimation made by Corvis ST highly depends on corneal thickness and tissue properties. As a consequence, the first applanation time may vary between patients with the same IOP due to differences in their corneal mechanical properties or geometries. Numerical simulations performed in our previous work [25] revealed that the first applanation does not generally coincide with the instant of maximum corneal velocity. The equilibrium point between internal and external forces does not necessarily occur when the cornea is flat. Instead, at the instant of maximum corneal apex velocity, the corneal acceleration is zero, indicating that the resultant force acting on the cornea is zero. This physical observation motivated the selection of the time of maximum velocity as the key feature for IOP estimation. To overcome these limitations, a novel methodology, developed concurrently within our group, was employed to compute patient-specific IOP. Equation (1) was derived from a novel energetic interpretation of the NCT process in Corvis ST, developed in our previous work [25]. To formalize this concept, FSI simulations of the Corvis ST air puff were employed. Unlike the Corvis ST device, which provides only the air pressure at the nozzle outlet, the FSI framework enables the computation of the actual pressure distribution on the corneal surface as it evolves in time and adapts to corneal deformation. Within this framework, an energetic balance was evaluated on the anterior corneal surface by comparing the work performed by the air puff and the work associated with the IOP. The intersection of these two energetic contributions identifies the equilibrium condition and corresponds to the instant of maximum corneal velocity. By systematically analyzing multiple simulations spanning physiologically realistic ranges of IOP, corneal thickness, geometry, and mechanical properties, a robust empirical relationship was identified between the time of maximum velocity and IOP. Patients' IOP was therefore computed using the derived Equation (1):

$$\begin{aligned}\text{wIOP [mmHg]} &= (-2.01 \cdot 10^{-3}) \cdot \text{time}^4_{\text{max-vel}} + (3.05 \cdot 10^{-2}) \cdot \text{time}^3_{\text{max-vel}} \\ &\quad + (2.99 \cdot 10^{-1}) \cdot \text{time}^2_{\text{max-vel}} - 3.15 \cdot \text{time}_{\text{max-vel}} + 10.95,\end{aligned} \tag{1}$$

where $\text{time}_{\text{max-vel}}$ is the time of maximum velocity of the corneal apex, provided by Corvis ST non-contact tonometer. This equation provides a numerical estimation of the IOP (called wIOP), which is independent of the mechanical properties of corneal tissue. The key assumptions underlying Equation (1) are that the energy balance is evaluated on the anterior corneal surface, neglecting thickness effects, and that the analysis is conducted along the optical axis for approximately symmetric corneal geometries; under these conditions, corneal mechanical properties do not influence the equilibrium condition at maximum velocity. The main limitations are that the formulation was developed on eyes with regular geometry, and that a direct in vitro experimental validation was initially missing. However, we are currently conducting an experimental validation of the proposed procedure, and preliminary results are very promising, further supporting the robustness and clinical relevance of Equation (1).

To predict the patient-specific mechanical properties of corneal tissue of the patients considered, the tool developed in our previous work was employed [22]. A reduced-order model (ROM), based on FSI simulations of the Corvis ST NCT, was created and used to generate training data for an ANN. Specifically, a feedforward ANN with neurons arranged into layers was adopted. A feedforward ANN establishes a mapping between the input space and the output space. This ANN formed the basis of a tool capable of estimating the parameters describing the mechanical behavior of corneal tissue in vivo. The inputs of the regression model were the coefficients of the reduced basis of the ROM, selected Zernike coefficients describing the anterior and posterior corneal surfaces, and the IOP (in this case, the wIOP). Conversely, the outputs of the network were the parameters describing the mechanical behavior of the corneal tissue. The strain energy density function (SEDF) selected for the development of the tool was the Holzapfel–Gasser–Ogden (HGO) constitutive model [26]. In this framework, since the epithelium contributes negligibly to corneal mechanical behavior, the corneal tissue was modeled as homogeneous throughout its thickness and anisotropic with two families of collagen fibers oriented perpendicularly to each other along the nasal-temporal and superior–inferior direction. This approach is widely used in the literature, given the predominant role of the stroma in determining corneal mechanical behavior and the limited availability of quantitative mechanical data for the other corneal layers [5, 6, 27, 28]. Therefore, following the assumptions adopted in our previous works [13, 14], the model geometry was defined by reducing the measured CCT by 50 μm (average epithelial thickness), to avoid overestimating the load-bearing stroma. Equation (2) reports the SEDF considered.

$$\psi(\overline{\mathbf{C}}, J, \mathbf{a}_0^4, \mathbf{a}_0^6) = C_{10}(\bar{I}_1 - 3) + \frac{k_1}{2k_2}\left(\sum_{i=4,6} e^{k_2(\bar{I}_i-1)^2} - 1\right) + \frac{1}{D}(\log J)^2 \tag{2}$$

where C_{10} [kPa] is a material parameter related to the extracellular matrix behavior, k_1 [kPa] refers to the stiffness of the fibers and k_2 [-] models their non-linearity. $\bar{I}_1$ is the first invariant of the right isochoric Cauchy–Green stress tensor, while $\bar{I}_4$ and $\bar{I}_6$ are, respectively, the fourth and the sixth pseudo-invariants related to the elongation of the fibers. Two families of collagen fibrils are assumed to be present in the corneal stroma with their mean (preferential) directions denoted by unit vectors $\mathbf{a}_0^4$ and $\mathbf{a}_0^6$, respectively, and one circumferential family at the limbus.

The tool leverages a dataset consisting of 140 corneal deformation images acquired over the 30-ms duration of the air puff applied by the Corvis ST device. In addition to these dynamic deformation images, the tool also takes as input the IOP (in this case the wIOP), and anterior and posterior corneal elevation maps obtained from Pentacam imaging. By integrating these data sources, the tool provides patient-specific estimations of corneal material parameters (C_{10}, k_1, k_2) in a non-invasive, patient-specific, and real-time manner. These parameters are estimated within pre-defined ranges, as the tool was trained using a synthetic dataset generated from FE FSI simulations of corneal deformation under NCT, spanning physiologically realistic ranges of material properties, geometry, and IOP. The network was validated using independent simulated data not employed during training, demonstrating good predictive accuracy and robustness.

Treatments Specifics for Clinical Validation

Tables 2-3-4 show the characteristics of the patients included in the study and the treatment specifics. The refraction reported in the tables follows the common notation used in clinics, indicating the sphere and the cylinder correction along with its axis ($S + C \times axis$). For all the patients, an optical zone of 6.5 mm for the ablation in PRK and LASIK and for the lenticule diameter in SMILE was considered, as indicated in the treatment plans. PRK and LASIK patients received *Wavefront-optimized* (also called *Standard*)

Table 2 Preoperative parameters of patients treated with PRK. Reported variables include Pentacam pre-surgical keratometry (Km pre), central corneal thickness (CCT), patient's refraction, central ablation depth (CAD), and residual stromal bed (RSB)

Patient	Km pre [D]	CCT [µm]	Refraction [D]	CAD [µm]	RSB [µm]
R01	42.8	590	−1.00−1.00×10°	34.39	556
R02	42.8	598	−1.00−1.00×140°	34.40	564
R03	43.5	513	−1.25−1.00×160°	41.72	471
R04	43.5	522	−1.00−2.50×0°	52.23	470
R05	44.1	515	−1.75−0.25×85°	34.42	481
R06	44.1	510	−2.00+0.00×0°	34.43	476
R07	43.2	514	−1.75−1.00×100°	45.47	469
R08	44.0	523	−2.00−1.25×70°	52.64	470
R09	43.0	534	−3.00+0.00×0°	49.16	485
R10	43.3	533	−3.00−0.25×10°	52.77	480
R11	45.1	582	−3.25−0.50×5°	56.38	526
R12	45.1	581	−3.75−0.50×0°	63.42	518
R13	43.8	565	−4.50+0.00×0°	67.09	498
R14	43.5	556	−4.00−0.25×0°	63.55	492
R15	43.1	521	−4.00−0.00×0°	59.98	461
R16	43.8	529	−4.25−0.00×0°	63.55	465
R17	45.6	522	−5.75−0.75×45°	87.87	434
R18	45.4	511	−3.25−1.25×95°	63.52	447
R19	43.2	483	−5.00−0.50×90°	68.91	414
R20	42.9	493	−5.00+0.00×0°	62.86	430

Table 3 Preoperative parameters of patients treated with LASIK

Patient	Km pre [D]	CCT [μm]	Refraction [D]	Flap ∅ [mm]	Flap Thickness [μm]	Hinge	CAD [μm]	RSB [μm]
R49	43.8	575	−1.50−1.75×10°	8.0	100	4.89 mm × 90°	52.73	422
R50	44.1	569	−1.25−1.75×15°	8.0	100	4.89 mm × 90°	49.11	420
R51	44.1	506	−1.25−3.50×30°	8.8	100	3.84 mm × 90°	63.55	342
R52	44.1	519	−1.00−4.00×160°	8.8	100	3.84 mm × 90°	63.36	356
R53	42.6	537	−2.00−1.25×135°	8.1	100	3.89 mm × 90°	52.67	384
R54	42.5	545	−2.50−1.25×50°	8.1	100	3.89 mm × 90°	59.93	385
R55	43.0	565	−2.25−0.25×90°	8.7	95	4 mm × 90°	41.77	428
R56	43.0	584	−2.25−0.25×80°	8.7	95	4 mm × 90°	41.82	447
R57	43.5	549	−3.75−0.75×175°	9.0	95	4 mm × 90°	67.07	387
R58	43.0	547	−3.00−0.25×30°	8.5	95	4 mm × 90°	49.16	403
R59	42.2	551	−2.75−1.00×110°	8.65	110	4 mm × 90°	56.23	385
R60	42.3	541	−2.00−0.50×160°	8.25	95	4 mm × 90°	41.74	404
R61	43.7	522	−2.25−0.50×0°	8.0	100	3.49 mm × 90°	41.71	380
R62	43.5	524	−4.50−0.50×150°	8.0	100	3.49 mm × 90°	74.13	350
R63	43.9	541	−4.00−0.75×160°	8.75	95	4 mm × 90°	70.15	376
R64	43.9	550	−3.50−1.00×15°	8.6	95	4 mm × 90°	74.06	381
R65	43.9	553	−5.75−0.25×10°	7.9	100	3.45 mm × 90°	78.24	375
R66	43.7	559	−5.25−1.25×175°	7.9	100	3.45 mm × 90°	87.76	371
R67	43.4	600	−5.50−1.50×165°	9.0	95	4 mm × 90°	98.03	407
R68	43.5	608	−5.75−0.75×5°	9.0	95	4 mm × 90°	91.34	422

Reported variables include pre-surgical Km, CCT, patient's refraction, flap diameter and thickness, hinge length and position, CAD and RSB

Table 4 Preoperative parameters of patients treated with SMILE

Patient	Km pre [D]	CCT [μm]	Refraction [D]	Cap ∅ [mm]	Cap Thickness [μm]	Incision	CAD [μm]	RSB [μm]
R21	42.4	514	−1.75−0.25×0°	7.6	120	2 mm × 120°	51	343
R22	42.3	516	−1.50−0.50×15°	7.6	120	2 mm × 120°	56	340
R27	42.6	516	−2.50−0.25×160°	7.6	120	2 mm × 120°	65	331
R28	42.9	515	−2.50−0.25×80°	7.6	120	2 mm × 120°	65	330
R29	42.9	542	−3.00−0.50×0°	7.6	120	2 mm × 120°	78	344
R30	42.6	536	−2.75−0.50×175°	7.6	120	2 mm × 120°	73	343
R31	43.0	557	−3.25−0.25×150°	7.6	120	2.32mm × 135°	78	359
R32	43.0	563	−3.25+0.00×0°	7.6	120	2.32mm × 135°	72	371
R33	45.1	551	−3.75−0.25×140°	7.6	160	2 mm × 120°	88	303
R34	45.1	550	−4.00+0.00×0°	7.6	160	2 mm × 120°	86	304
R35	43.0	529	−4.50−0.50×0°	7.6	160	2 mm × 120°	103	266
R36	42.9	524	−4.50−0.50×10°	7.6	160	2 mm × 120°	103	261
R37	42.8	553	−5.00−0.25×30°	7.5	120	2.5mm × 120°	106	327
R38	42.9	557	−5.00−0.25×0°	7.5	120	2.5mm × 110°	107	330
R39	46.9	573	−4.75−0.25×55°	7.6	160	2 mm × 120°	107	306
R40	46.8	572	−4.75−0.25×120°	7.6	120	2 mm × 120°	105	347
R41	45.4	593	−5.25+0.00×0°	7.6	120	2 mm × 120°	106	367
R42	45.6	583	−6.00+0.00×0°	7.6	120	2 mm × 120°	118	345

Reported variables include pre-surgical Km, CCT, patient's refraction, cap diameter and thickness, incision length and position, CAD and RSB

treatment). The VisuMax user manual does not disclose the algorithm used to define the SMILE lenticule shape, therefore, for modeling purposes, we treated it as equivalent to the PRK/LASIK wavefront-optimized algorithm.

In-silico Models of Refractive Treatments

Patient-specific FE models were built as described in our previous work [13], using data acquired with the Pentacam topographer.

Unlike in silico simulations of NCT, which involve large deformations and necessitate the inclusion of the sclera in the model due to its substantial mechanical contribution, simulations of laser refractive procedures are characterized by displacements and strains that are smaller in magnitude. Nevertheless, all simulations are performed within a geometrically nonlinear, large-deformation framework. Under these conditions, the sclera can be excluded from the finite element model without compromising accuracy, provided that appropriate boundary conditions are imposed [13]. In this work, boundary conditions were applied at the limbus, constraining the nodes to radial displacements only, within a spherical coordinate system centered at the origin of the best-fit sphere to the corneal geometry (see Figs. 1-3).

Patient-specific material properties were estimated for each eye included in the study using the methodology described in Sect. 2.3 and given as input to the models (see Table 9 in the Appendix). To ensure consistency with the constitutive model used to train the ANN, the same SEDF was employed (Equation (2)).

The FE model wee discretized using 0.1 mm quadratic tetrahedral elements, generated in ANSA (v22.0.1, BETA CAE Systems). Regarding the loading conditions, IOP was modeled as a constant pressure load applied uniformly to the posterior surface of the corneal model. Since the eye is under physiological IOP during topographic data acquisition, the measured geometry corresponds to a deformed configuration, with the actual deformation field unknown. Therefore, before performing any biomechanical simulation of a pressure-loaded biological structure, it is essential to recover the initial unpressurized configuration. To this end, an in-house iterative algorithm was employed to estimate the unpressurized reference geometry, as described in [29]. Once the reference configuration is recovered, the refractive intervention can be simulated.

To accurately simulate a refractive procedure, the ablation profile must be precisely defined and incorporated into the model's mesh prior to simulation. The algorithm used to compute the ablation profile is proprietary to the laser manufacturer and is not publicly accessible. However, each patient's treatment plan provides key information regarding the algorithm employed (e.g., wavefront-optimized, wavefront-guided, topography-guided) and includes the corresponding ablation map, which specifies the spatial distribution of tissue removal across the corneal surface. To replicate the clinical ablation profile, we developed an in-house algorithm inspired by the wavefront-optimized method proposed by [30]. Nevertheless, as shown in our previous work [13], existing theoretical algorithms, including that of Mrochen, tend to underestimate the CAD, which is a parameter critical for achieving accurate optical outcomes. To address this limitation, the proposed algorithm applies a calibration step in which the theoretical ablation profile is adjusted to reproduce the CAD specified in the patient's treatment plan. This

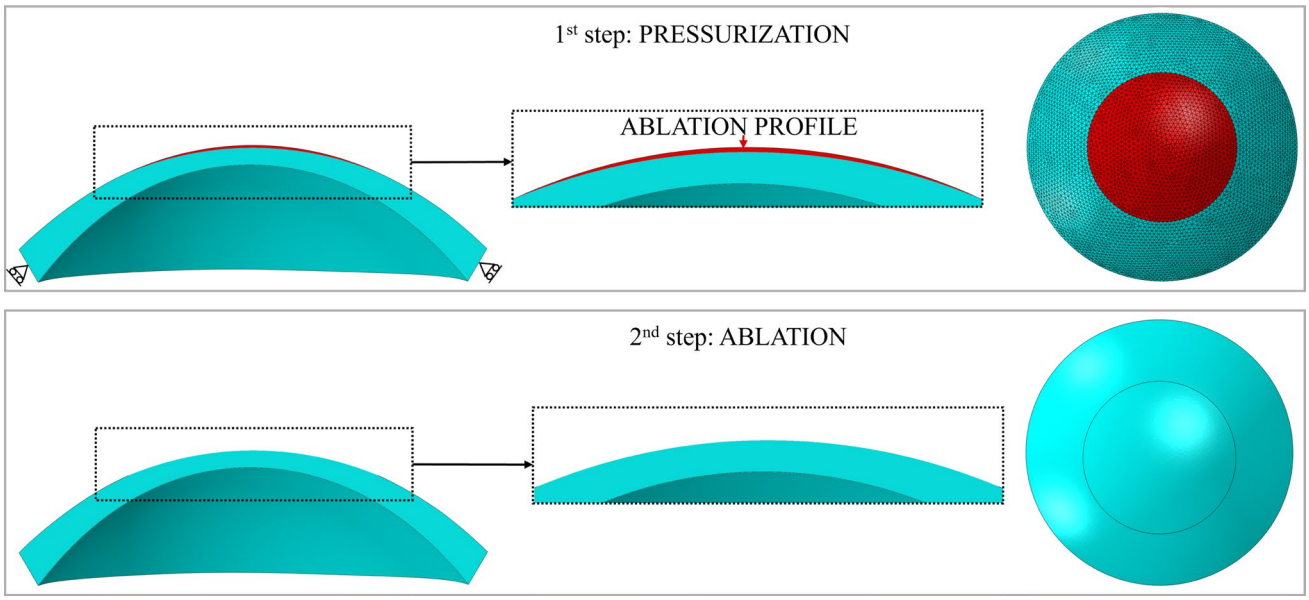

Fig. 1 PRK surgery simulation

ensures that the simulated ablation depth at the corneal center matches the clinically prescribed value, while preserving the spatial distribution predicted by the analytical formulation.

All the simulations were run with the proprietary software ABAQUS 2022 (Dassault Systèmes Simulia Corp., Providence, RI, USA). When constructing the FE model, specific adjustments must be made depending on the selected surgical procedure.

PRK

In the PRK model, two separate element sets are defined to distinguish the ablation volume from the remaining post-surgical corneal tissue. Patients' refraction and CAD are reported in Table 2. PRK surgery is simulated in two steps (Fig. 1):

- *Step 1 – Pressurization*: The model is pressurized by applying the IOP to the posterior surface of the cornea.
- *Step 2 – Ablation*: The ablation volume is removed to replicate the surgical tissue removal.

LASIK

During LASIK, a hinged flap is cut in the cornea and lifted, enabling direct laser ablation of the underlying stromal layer. Flap dimensions, hinge position, refraction, and CAD for each patient are presented in Table 3.

Before running the simulation, specific contact definitions must be established between parts of the corneal geometry. These contacts are activated or deactivated depending on the simulation step:

- *Rough contact between pre-surgical cornea and flap*: A rough contact is defined between the bottom surface of the flap and the underlying corneal surface to ensure model continuity at the initial condition. This is necessary because the flap and the residual cornea are imported separately, resulting in duplicated nodes. The contact is modeled as hard contact with infinite friction (i.e., rough contact) to prevent sliding and penetration between surfaces. It is active during the pressurization step.
- *Frictionless contact between post-surgical cornea and flap*: A frictionless contact is pre-defined to represent the post-surgical condition, in which the flap comes into contact with the ablated corneal surface. This contact is also modeled as hard contact, but without friction, allowing sliding while avoiding penetration. It is activated in the second step, after the ablation volume is removed.
- *Tie constraint at the flap hinge*: The flap hinge, which remains uncut during surgery, is tied to the rest of the cornea to preserve continuity in this region throughout the simulation.

LASIK surgery is simulated in three steps (Fig. 2):

- *Step 1 – Pressurization*: The model is pressurized by applying the IOP to the posterior surface of the cornea. During this step, only the rough contact is active.

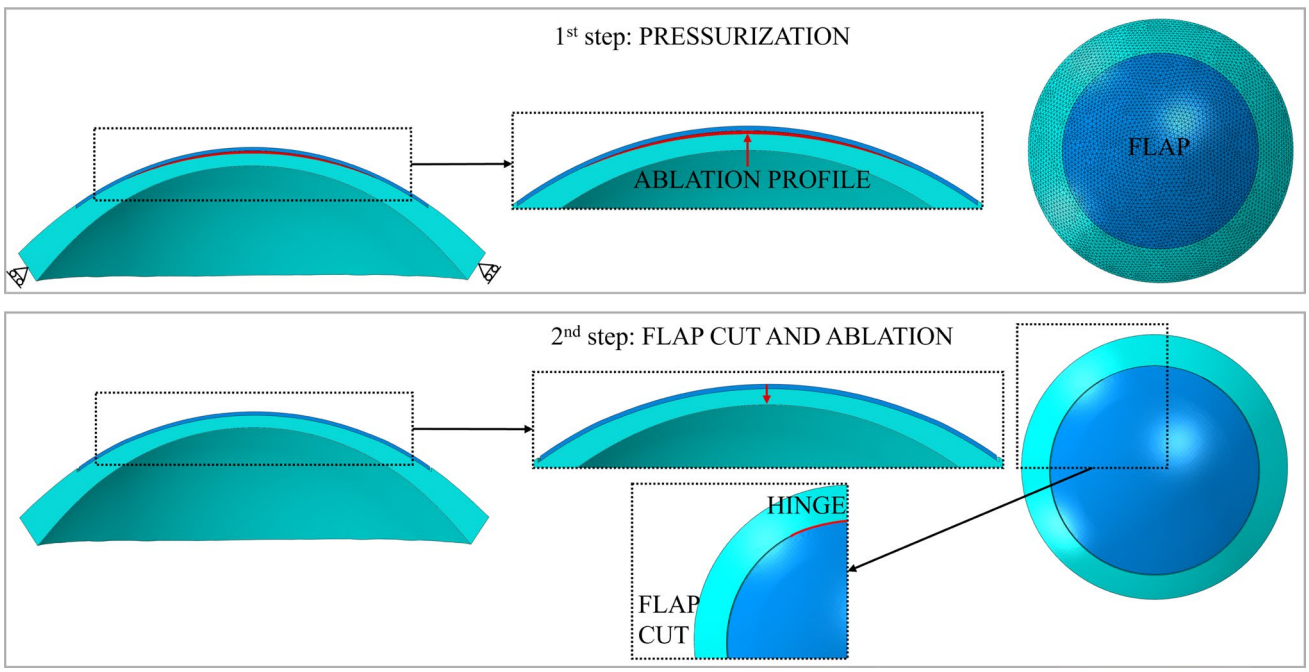

Fig. 2 LASIK surgery simulation

- *Step 2 – Flap cut and ablation*: The flap is virtually cut by deactivating the previously defined contact between the flap and the underlying cornea. The ablation volume is then removed, and a superficial pressure of $P = 0.1$ mmHg is applied to the flap to push it downward, promoting contact between the flap's bottom surface and the post-surgical corneal surface.
- *Step 3 – Equilibrium*: The superficial pressure P is removed, allowing the model to reach its equilibrium configuration.

SMILE

All model parameters, including cap dimensions, incision length and position, refraction, and CAD for each SMILE patient are presented in Table 4. In daily clinical practice, an additional 10% is added to the target correction during SMILE to ensure optical accuracy. Furthermore, 15 µm of thickness is added to the lenticule to prevent rupture during surgical extraction [31]. For these reasons, the CAD in SMILE treatment is greater than that in PRK and LASIK.

Before running the simulation, several contact interactions between parts of the corneal geometry must be defined. These contacts are activated or deactivated depending on the simulation step:

- *Rough contact between pre-surgical cornea and cap*: As in the LASIK model, a rough contact is defined between the bottom surface of the cap and the underlying corneal surface to ensure model continuity at the initial condition. The interaction is modeled as hard contact with infinite friction to prevent sliding and interpenetration between surfaces. It is active during the pressurization step.
- *Frictionless contact between post-surgical cornea and cap*: A frictionless contact is pre-defined to represent the post-surgical condition, where the bottom surface of the cap comes into contact with the stromal surface exposed after lenticule removal. This is modeled as hard contact with no friction to allow sliding while preventing penetration. It is activated in the second step, once the lenticule has been removed.
- *Tie constraint at the edge of the cap*: The edge of the cap, which remains uncut during the procedure, is tied to the rest of the cornea to maintain structural continuity throughout the simulation.
- *Rough contact at the incision site between corneal and cap edges*: A rough contact is defined at the interface between the edges of the cap and the cornea at the incision site. This contact is active during the pressurization step but is deactivated after lenticule removal to simulate the surgical incision.

SMILE surgery is simulated in two steps (Fig. 3):

- *Step 1 – Pressurization*: The model is pressurized by applying the IOP to the posterior surface of the cornea.
- *Step 2 – Lenticule extraction*: The lenticule is removed, and a hard, frictionless contact is activated to prevent penetration between the two internal corneal surfaces that come into contact under the effect of IOP. Simul-

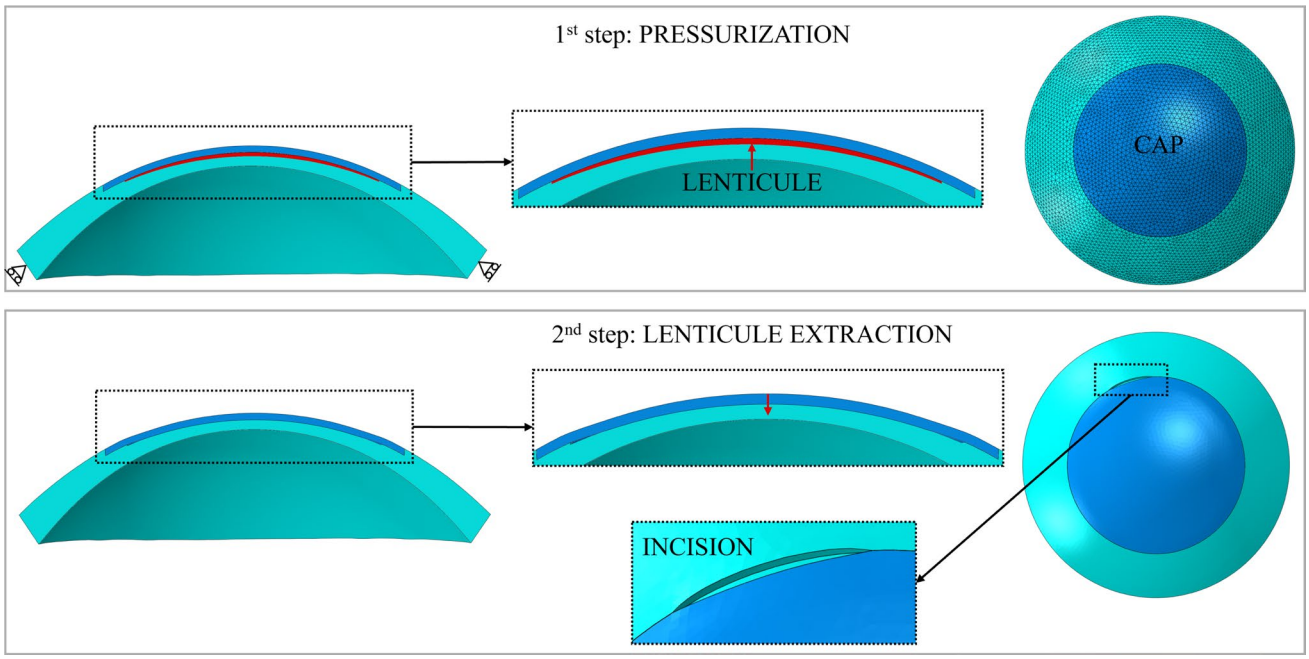

Fig. 3 SMILE surgery simulation

taneously, the contact at the incision site is released to simulate the surgical cut.

Optical Analysis for Methodology Validation

In clinical practice, distance best-corrected visual acuity (DBCVA), that is patient's subjective refraction, is computed to determine patient's vision quality and assess whether a treatment has successfully corrected the existing defect. Given the impossibility to evaluate subjective refraction in FE models, simulated keratometry (SimK) was used in this work as an objective metric to assess the refractive outcome of the simulations. SimK quantifies changes in corneal curvature, specifically reflecting changes in the corneal geometry. To compute SimK values in the FE models, the principal curvatures (K1 and K2) and their mean (Km) were calculated using a biconic fitting approach from [32], considering an optical zone diameter of 3 mm, which corresponds to the one used in clinics for keratometric calculations [33, 34]. Since curvature in ophthalmology is commonly expressed in diopters (D) [1/m] to account for the refractive index difference between air and the cornea, the computed mean curvature is converted as follows:

$$Km\ [D] = (n_{KI} - n_{air})\frac{1}{Rm}, \tag{3}$$

where Rm is the mean apical radius, $n_{air} = 1$ is the refractive index of air, and $n_{KI} = 1.3375$ is the corneal keratometric refractive index—a simplified effective index that accounts for the negative optical power introduced by the posterior corneal surface [35]. This modified refractive index is used in the calculation of keratometric values, such as SimK. To validate the methodology and evaluate its accuracy, pre- and post-surgical Km values obtained from the FE models were compared with those from Pentacam clinical examinations.

Astigmatic outcomes were evaluated using the Alpins method for vector analysis of astigmatism [36] to quantitatively compare intended, clinically achieved, and numerically predicted astigmatic corrections. Accordingly, the Target-Induced Astigmatism (TIA), defined as the intended astigmatic correction specified in the patient's surgical treatment plan, and the Surgically Induced Astigmatism (SIA), derived from clinical and numerical outcomes, were computed. For clarity, the equations used in this analysis are reported in the Appendix. TIA was obtained from the astigmatic component of the manifest refraction reported in the surgical treatment plan, using the prescribed cylinder magnitude and axis. SIA was computed from keratometric data obtained from Pentacam measurements, both clinically (pre- to postoperative) and numerically (pre- to post-simulation). Manifest refraction could not be evaluated for the finite element simulations; therefore, keratometric data were used consistently to quantify both clinical and simulated SIA. For consistency, astigmatism was expressed using the flat keratometric meridian convention, which is standard for Pentacam outputs and was also adopted for the finite element simulations. Vector calculations were performed in power-vector space (J0, J45), from which astigmatic magnitudes and axes were reconstructed. Standard Alpins metrics were then computed, including the Correction Index (CI) and Difference Vector (DV). To avoid instability in ratio-based metrics, CI was reported only for cases with TIA ≥ 0.50 D.

Results

The following section provides a thorough description of the main results to validate the proposed methodology for patient-specific refractive surgery simulation.

Estimation of Patient-Specific Material Properties

Table 5 shows the mean, standard deviation, minimum, maximum, and the 25th, 50th (median), and 75th percentiles for the patients specific material properties and wIOP, estimated with the methodology described in Sect. 2.3.

To assess whether the estimated mechanical properties are consistent with the clinically observed deformation behavior, we analyzed Corvis ST outputs—specifically deflection amplitude, bIOP, SSI, and pachymetry—alongside the estimated material parameter k_2 across the patient cohort. The parameter k_2 plays a dominant role in governing the material's behavior under high-strain conditions, making it particularly relevant for characterizing corneal stiffness. For this reason, we started our analysis from k_2, and Table 6 reports the mean values of selected Corvis ST outputs for the two extreme subgroups: patients with k_2 values below the 10^{th} percentile and those above the 90^{th} percentile.

Corneas with low estimated k_2 values (below the 10^{th} percentile) showed higher deformation (mean deflection amplitude: 1.18 mm). Conversely, corneas with high k_2 values exhibited reduced deflection amplitudes (mean: 1.07 mm), consistent with stiffer tissue behavior. Notably, corneas with low k_2 also had a lower mean SSI (0.87), while those with

Table 5 Ranges of the estimated patient-specific mechanical properties and wIOP

	mean ± std (min/max)	25%	50%	75%
wIOP [mmHg]	10.24 ± 1.33 (8.93/16.1)	9.53	10.15	10.20
C_{10} [kPa]	59.4 ± 27.5 (14.9/112.0)	36.9	53.2	79.6
k_1 [kPa]	125.1 ± 7.48 (92.62/130.0)	124.6	128.3	129.7
k_2 [-]	936.8 ± 176.6 (226.0/998.0)	990.25	997.49	998.00

For each variable the mean, standard deviation (std), minimum value (min), maximum value (max), and 25, 50, and 75 percentiles are reported

Table 6 Analysis of the variables with respect to the value of k_2

	mean
(a) Mean of the variables among patients with low k_2. (patients with k_2 below 10 percentile)	
bIOP [mmHg]	13.83
wIOP [mmHg]	9.75
Pachy [μm]	556.50
Age [years]	32.2
Def. Amp. Max [mm]	1.18
SSI [-]	0.87
C_{10} [kPa]	65.0
k_1 [kPa]	121.9
k_2 [-]	480.66
(b) Mean of the variables among patients with high k_2. (patients with k_2 above 90 percentile)	
bIOP [mmHg]	15.36
wIOP [mmHg]	10.30
Pachy [μm]	545.19
Age [years]	33.7
Def. Amp. Max [mm]	1.07
SSI [-]	1.01
C_{10} [kPa]	58.7
k_1 [kPa]	125.5
k_2 [-]	989.43

high k_2 showed a higher mean SSI (1.01), suggesting a similar trend in stiffness estimation as assessed by the Corvis.

Among the studied cohort, four eyes (IDs: **13, 14, 41, 51**) had estimated $k_2 < 500$. They correspond to the most compliant curves in Fig. 4.

Eyes with IDs 13 ($k_2 = 344$) and 14 ($k_2 = 452$), corresponding to the right and left eyes of the same patient, demonstrated high deflection amplitudes (1.188 mm and 1.221 mm) and low SSI values (0.865 and 0.847). Both biomechanically corrected intraocular pressure (bIOP) and pachymetry were close to the population mean. The combination of low k_2, low SSI, and pachymetry and bIOP near the mean values indicates a compliant corneal response and suggests consistency between our estimated material parameter and the SSI parameter from Corvis.

Eye with ID 41 ($k_2 = 226$) follows a similar pattern, with a deflection amplitude of 1.240 mm, very low SSI (0.657) but also low bIOP (11.8 mmHg). In this case, the high deflection amplitude can be attributed to the combined effect of a intraocular pressure lower than the mean and compliant

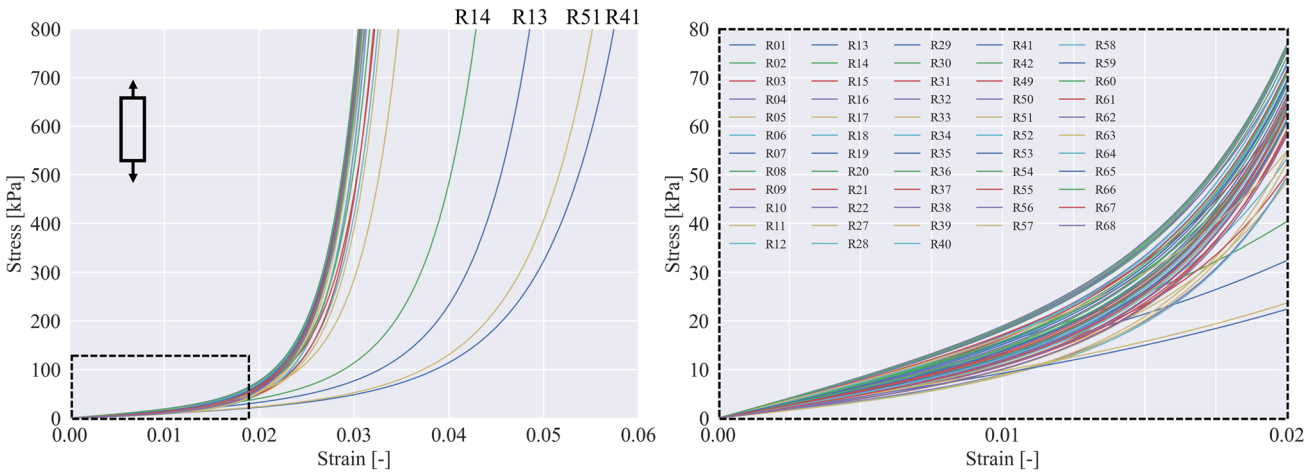

Fig. 4 left: uniaxial stress–strain curves computed by evaluating the constitutive model using the material parameters identified by the ANN; right: zoomed-in view of the stress–strain range reached in the simulations

mechanical properties, both of which contribute to increased corneal deformability.

Eye with ID 51 ($k_2 = 252$) exhibited a high deflection amplitude (1.279 mm), low pachymetry (506 µm), and bIOP of 12.8 mmHg, again suggesting compliant behavior of the corneal tissue. In this case, its SSI was near the mean (0.913).

Only 4 eyes (IDs: **11, 12, 31, 54**) had intermediate values of k_2 with $500 \leq k_2 \leq 900$. All remaining eyes in the cohort had $k_2 > 900$. For this reason, the stress–strain curves for these patients in Fig. 4 show similar behavior.

Finally, eyes with IDs 19 and 20 showed high deflection amplitudes but also exhibited very low pachymetry. In these cases, the estimated k_2 values were not low, indicating that the observed deformation was primarily due to corneal thinness rather than inherent material compliance.

The mean error in the prediction of the parameters by the ANN was 8.40% for C_{10}, 36.17% for k_1, and 27.78% for k_2. Across all patients, the estimated values of k_1 were found to be relatively close to each other, with the 25th and 75th percentiles being 124.6 kPa and 129.7 kPa, respectively. As previously discussed in [22], k_1 has only a minor influence on the outcomes of NCT simulations. For this reason, the relatively higher prediction error observed in the ANN for this parameter can be considered acceptable. Figure 4 shows analytically derived uniaxial stress–strain curves illustrating the inter-patient variability in the HGO SDEF (Eq. 2) material parameters identified by the ANN. A zoomed-in view of the curve, focusing on the region of interest where the refractive surgery simulations work (as it will be shown in Subsection 3.3), is also shown.

Clinical Validation of the FE Methodology for Refractive Surgery Simulation

Figure 5 shows the comparison of subjective refraction (DBCVA), expressed as spherical equivalent, between pre- and post-surgical clinical scenarios for the patients included in the study. A clear reduction—or complete elimination—of the refractive error is observed in the majority of patients. In some cases, a residual error within ±1 D remains consistent with the findings reported in the literature [4].

Figure 6, instead, presents the simulated spherical change plotted against the clinical spherical change derived from Pentacam data. The spherical change was calculated as the difference in Km between pre- and post-surgical conditions. While this metric does not represent the actual refractive correction—typically assessed through subjective refraction in clinical settings—it provides an estimate of curvature change, enabling evaluation of the simulation error. For clinical spherical changes between 2 and 4 D, the simulations closely matched the clinical data, with errors within ± 0.5 D and a tendency towards undercorrection. However, for clinical spherical changes greater than 4 D, the simulation error increased up to ±1 D, indicating reduced accuracy of the methodology in these cases.

Going into the details of each scenario (pre-surgical vs. post-surgical, Tables 10–11 (see Appendix)), the SimK values obtained from Pentacam clinical data and the FE model under pre- and post-surgical conditions are compared for the selected patients. Only the error in Km is reported, as it is the most influential parameter affecting the final optical quality. The error was computed as the difference between the simulated and clinical values, with the latter serving as the reference.

Preoperatively, the mean spherical error of our models relative to clinical measurements was $+0.10 \pm 0.10$ D. This bias likely reflects uncertainties introduced by the patient-specific geometry reconstruction. Postoperatively, the mean error increased to $+0.40 \pm 0.30$ D. Given the micrometer-level accuracy required and the deformations occurring in the FE simulations, this magnitude remains acceptable and indicates a slight undercorrection relative to the clinical outcomes.

Regarding astigmatism (cylinder) correction, Table 7 reports a summary of Alpins vector analysis metrics.

Since TIA directly reflects the magnitude of the preoperative astigmatism targeted for correction, the observed differences among groups are expected and simply mirror the distribution of preoperative cylinder in our cohort. Accordingly, higher TIA values were found in LASIK (1.15 ± 1.01 D), intermediate values in PRK (0.60 ± 0.64 D), and lower values in SMILE (0.26 ± 0.18 D), consistent with the

Table 7 Summary of Alpins vector analysis metrics (mean ± SD) for clinical and simulated astigmatic outcomes across refractive procedures

Group	n	n_{CI}	TIA [D]	SIA [D]		DV [D]		CI [-]	
				Clinical	Simulated	Clinical	Simulated	Clinical	Simulated
PRK	20	10	0.60 ± 0.64	0.86 ± 0.49	0.75 ± 0.66	1.42 ± 1.10	1.32 ± 1.25	1.28 ± 0.46	1.20 ± 0.56
LASIK	20	16	1.15 ± 1.01	1.16 ± 0.80	1.14 ± 0.96	2.28 ± 1.79	2.24 ± 1.94	1.10 ± 0.42	1.06 ± 0.64
SMILE	18	4	0.26 ± 0.18	0.37 ± 0.20	0.30 ± 0.17	0.60 ± 0.25	0.51 ± 0.24	0.45 ± 0.33	0.40 ± 0.43

TIA: Target-Induced Astigmatism; SIA: Surgically Induced Astigmatism; DV: Difference Vector; CI: Correction Index. n indicates the total number of eyes per group; n_{CI} indicates the number of eyes with TIA ≥ 0.50 D included in CI computation (to avoid instability of ratio-based metrics for very small intended cylinder). TIA, SIA, and DV are reported for the full cohort (n), whereas CI is reported for the subset (n_{CI})

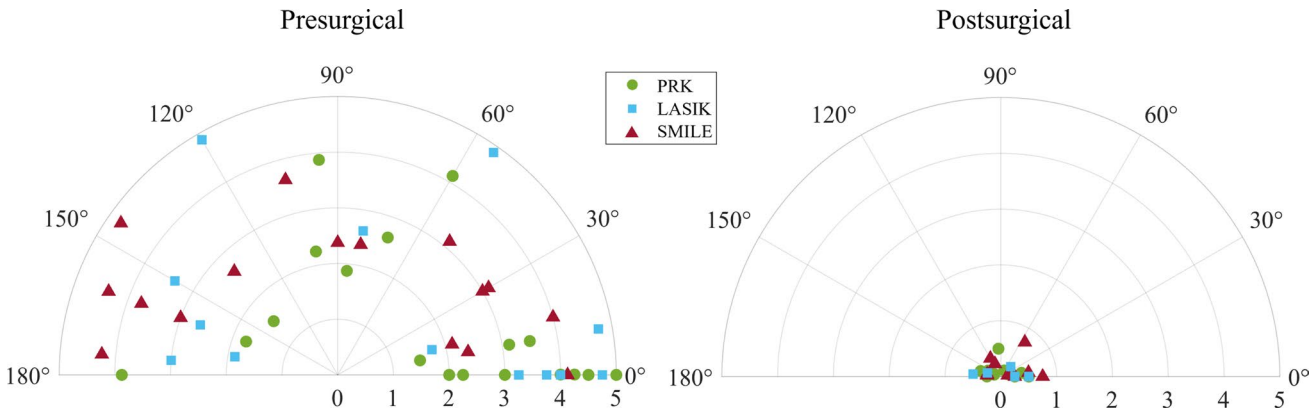

Fig. 5 Pre- and post-surgical clinical spherical equivalent of patients' subjective refraction.

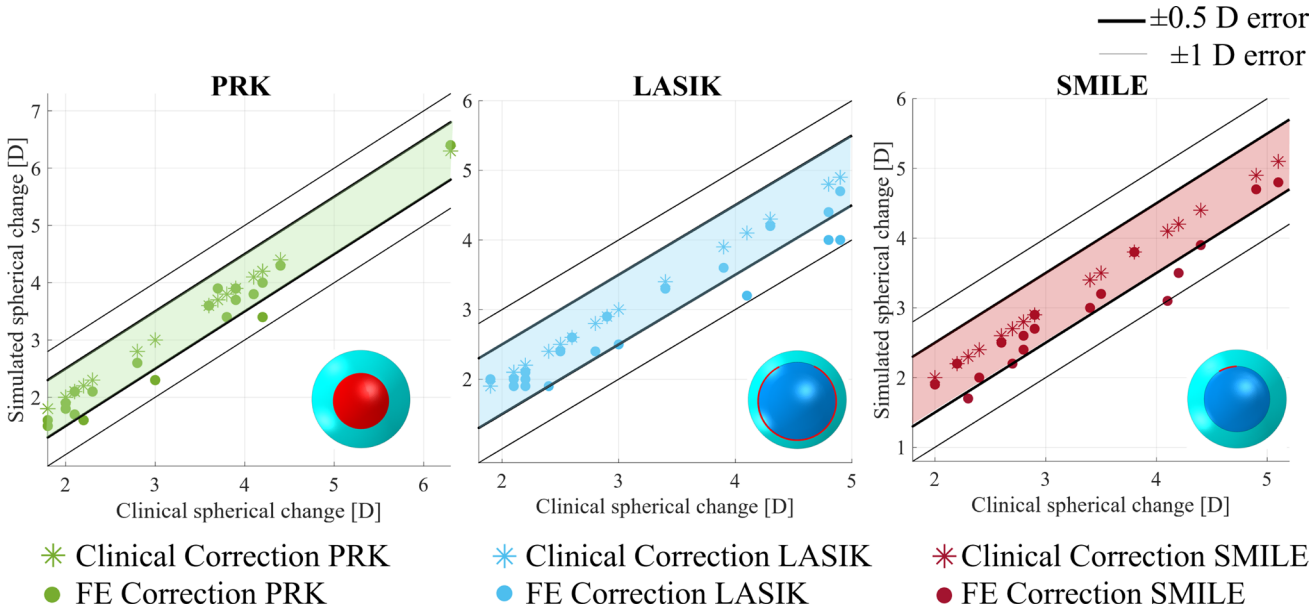

Fig. 6 Clinical vs. simulated spherical change in patients. The spherical change was computed as the difference between pre-surgical and post-surgical Km for both clinical and simulated scenarios.

smaller intended astigmatic corrections typically prescribed in SMILE candidates.

Vector analysis demonstrated a good agreement between clinically measured and numerically predicted astigmatic outcomes across all refractive procedures. Group-wise results (mean ± std) showed comparable mean SIA magnitudes between clinical and simulated data for LASIK (1.16 ± 0.80 D vs. 1.14 ± 0.96 D), PRK (0.86 ± 0.49 D vs. 0.75 ± 0.66 D), and SMILE (0.37 ± 0.20 D vs. 0.30 ± 0.17 D). This correspondence is further illustrated in Fig. 7, which shows a strong correspondence between clinically measured and numerically predicted SIA magnitudes across procedures, with most data points clustering around the line of identity. As expected, dispersion increases at lower TIA (smaller intended corrections), with clinical measurements tending to exhibit slightly higher SIA than simulations in that range.

To avoid instability of ratio-based indices when TIA is very small, CI was computed only for eyes with TIA ≥ 0.50 D (the number of cases per group is reported as n_{CI} in Table 7). Under this restriction, CI values were close to unity for LASIK and PRK, indicating an overall appropriate correction magnitude. Lower CI values in SMILE should be interpreted with caution given the very small subset size ($n_{CI} = 4$) and the smaller intended corrections in this group; they reflect a modest undercorrection in those specific cases and the greater sensitivity of CI at low TIA, rather than a systematic planning deficiency. DV magnitudes were

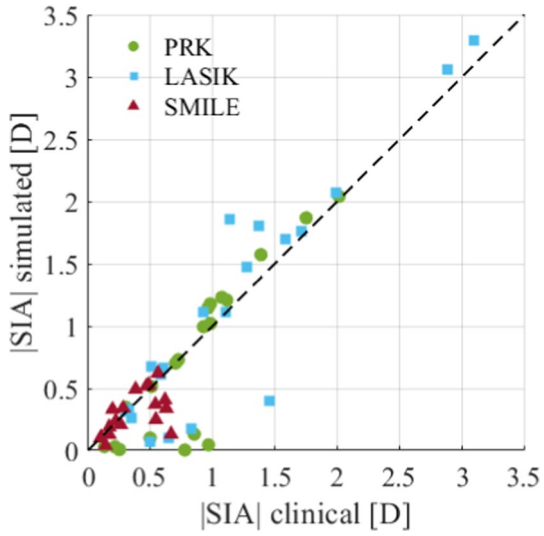

Fig. 7 Comparison between measured (Pentacam) and numerically predicted (FE) SIA magnitudes. Results are shown for PRK, LASIK, and SMILE procedures. The dashed line represents the line of identity.

comparable between clinical and simulated outcomes, suggesting a similar residual astigmatic error pattern in both datasets. We note that DV did not approach zero, likely because SIA was computed from keratometric data rather than manifest refraction, which are not directly equivalent.

Overall, the vector analysis confirms that the proposed simulation framework is able to reproduce not only the magnitude but also the directional characteristics of surgically induced astigmatism observed clinically, supporting its potential use for predicting astigmatic outcomes in refractive surgery planning.

Mechanical Comparison Among the Treatments

Three eyes (R13, R62, and R35) with similar refractive defects (see Tables 2-4) were selected for comparison from a mechanical perspective. Each selected patient underwent a different treatment: eye R13 underwent PRK, eye R62 LASIK, and patient R35 SMILE. The features of the eyes selected for the comparison are summarized in Table 8 for clarity.

Figure 8 shows the pre- and post-surgical distribution of the maximum principal stress and logarithmic strain in the three eyes. In the pre-surgical scenario, subtle differences in both stress and strain distributions can be observed at the posterior surface of the models. These differences arise from variations in the mechanical properties and geometries of the patients' corneas. In the post-surgical scenario, the mechanical impact that each treatment has on corneal tissue becomes evident.

Of the three procedures, PRK was the least mechanically invasive, producing the smallest increases in RSB stress and strain (21.0% and 17.7%, respectively), relative to the preoperative state. LASIK had an intermediate effect, raising RSB stress and strain by 48.2% and 30.7% with respect to pre-surgical state; additionally, anterior-surface stresses decreased because the flap is largely mechanically unloaded after its creation. By contrast, SMILE produced the largest changes, with RSB stress and strain increasing by 68.2% and 48.8%, respectively, relative to pre-surgical conditions.

Regarding the strains, SMILE seems to deform more the geometry, affecting a larger volume of the RSB.

In all the three treatments, post-surgical strains generated in the models vary between 0.7% and 0.1%, that represent the range of interest in our simulations, as pointed out in Fig. 4.

Discussion

In this work, a detailed methodology for patient-specific simulation of laser refractive treatments has been presented and validated, including individualized material properties and IOP. To estimate the patient-specific mechanical properties of the corneal tissue, the tool developed in [22] was employed. This tool takes Corvis ST images, Pentacam data, and IOP as input and returns the material parameters of the HGO constitutive model as output, which are then given as input to the FE corneal model. While the IOP estimated by the Corvis ST can also be used as input, it was deliberately excluded in this work because its estimation depends on both the corneal mechanical properties and the patient-specific geometry resulting in a coupling between IOP and corneal biomechanics [25]. To address this limitation, the IOP was instead computed using Equation (1), which is based on the time of maximum corneal apex velocity measured by the Corvis ST. This parameter is independent of both material properties and corneal geometry, thereby allowing the decoupling of IOP and corneal biomechanics.

Table 8 Characteristics of the three eyes of the patients selected for the comparison

	CCT [μm]	C_{10} [kPa]	k_1 [kPa]	k_2 [-]	IOP [mmHg]	CAD [μm]	RSB [μm]
R13	565	78	116	344.5	10.2	67.09	498
R62	519	103.2	128.7	997.8	10.2	74.13	345
R35	529	78.1	129.2	983.8	10.2	103	266

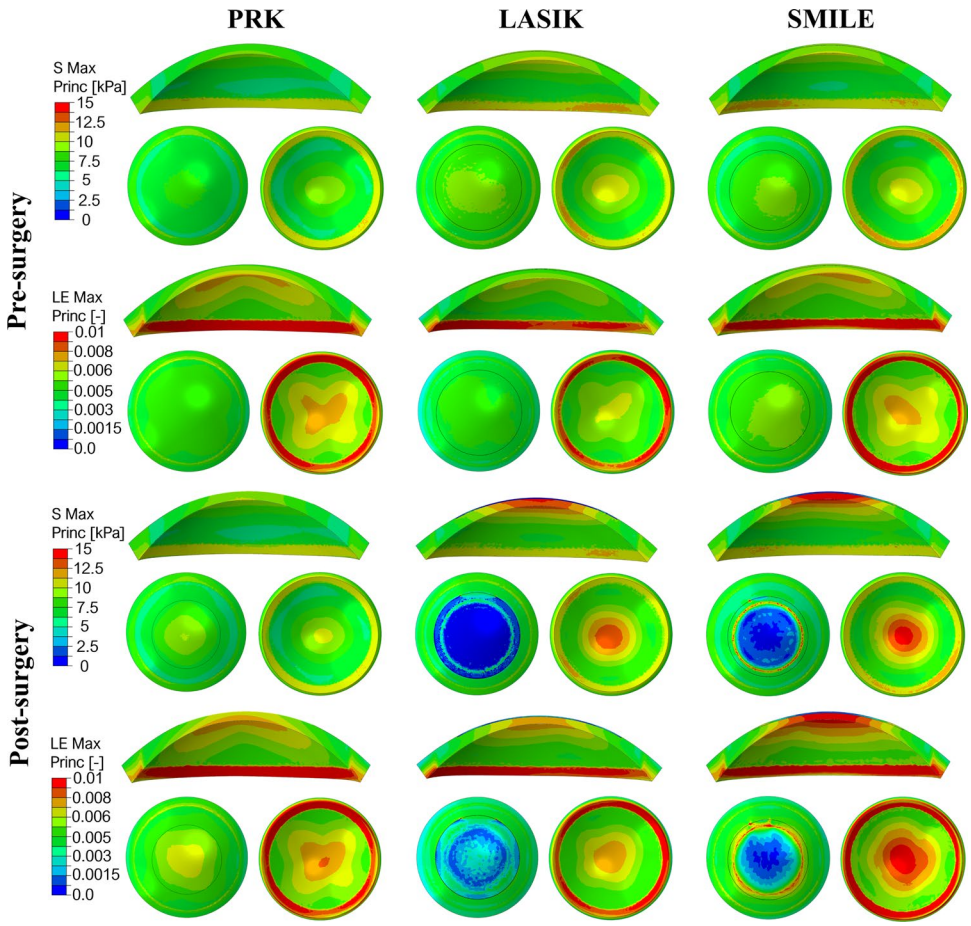

Fig. 8 Pre- and post-surgical distributions of maximum principal stress and logarithmic strain in three patients, one who underwent PRK (R13), one LASIK (R62), and one SMILE (R35).

The proposed methodology for laser refractive surgery simulation proved to be accurate for dioptric correction between -2 D and -4 D, showing a mean error within ±0.5 D. However, the optical accuracy of the methodology decreased at high dioptric corrections ($\geq -4D$), displaying an error within ±1 D. This is likely due to the fact that, for higher dioptric corrections, a thicker portion of corneal tissue is removed, and the model's mechanical response becomes more pronounced, being subjected to higher geometrical deformations. As a result, high dioptric corrections require greater accuracy both in the model and in the estimation of its material parameters.

To increase the accuracy of the properties estimation, the error in parameter estimation should be minimized, therefore enhancing the tool through an expanded training dataset. In fact, the mean error in the prediction of the parameters was 8.40% for C_{10}, 36.17% for k_1, and 27.78% for k_2. The overall mechanical response, as shown in the stress–strain curves (Fig. 4), was largely consistent across patients. The few subjects that deviated more noticeably have been specifically discussed in Sect. 3.1. It is important to note that the relatively high error on k_1 has negligible impact, since this parameter contributes minimally to corneal deformation. Indeed, the predicted values of k_1 exhibited limited variability (ranging from 92 to 130). Similarly, k_2 values were generally high, with only four exceptions that were analyzed in more detail in Sect. 3.1. The parameter showing the most variability was C_{10} (ranging from 14 to 112). As demonstrated in section 3.3, the range of interest in our simulations corresponds to the linear portion of the stress–strain curve, governed by C_{10}, which captures the behavior of the extracellular matrix (ECM). Therefore, lowering the error in the C_{10} prediction could improve the accuracy in the post-surgical results of the surgery simulations.

The tool for the estimation of the mechanical properties of the corneal tissue was validated with FSI simulations of the corneal deformation during an air puff [22]. In that case, the error in the prediction of the material parameters did not consistently affect the accuracy of the FSI simulation, as these simulations capture the global mechanical response of the eye, where minor variations in property estimation are not significant. However, when this tool is applied to refractive treatment simulations, a higher level of accuracy is required, and the prediction error of the ANN has a greater impact on the optical accuracy of the simulations.

The Alpins vector analysis further supports the validity of the proposed framework by demonstrating that the numerical model is able to reproduce not only the magnitude but also

the directional characteristics of surgically induced astigmatism observed clinically. The correspondence between clinical and simulated SIA across PRK, LASIK, and SMILE suggests that the biomechanical and geometric changes induced by the simulated ablation profiles are realistically captured. While the analysis relies on keratometric data for SIA, due to the lack of manifest refraction outputs in the numerical simulations, this choice is consistent with the objective comparison of corneal shape changes and is commonly adopted in refractive surgery studies [10]. In this context, DV should be interpreted with caution (Table 7) because TIA is defined from the planned manifest refraction (treatment plan), whereas SIA is derived from Pentacam keratometry, DV does not represent a purely refractive residual and may remain far from zero even when postoperative refractive outcomes are clinically acceptable. This reflects the fact that keratometric and manifest refractive astigmatism are not directly interchangeable and can differ. Accordingly, DV absolute magnitude in this study should not be interpreted as a direct measure of planning quality; rather, their relevance here is that clinical and simulated DV are comparable, indicating that the model reproduces the residual keratometric astigmatic pattern observed clinically. Reduced reliability for very small intended corrections was addressed by excluding low-TIA cases from ratio-based metrics, in line with standard recommendations for vector analysis.

Finally, three patients who underwent PRK, LASIK, and SMILE treatments, respectively, were selected to perform a mechanical analysis of the impact of each surgery on the model. SMILE proved to be the most invasive treatment from a mechanical perspective, despite considering three different patients with their unique tissue properties. SMILE surgery was introduced into clinical practice because it is commonly believed to be less mechanically invasive than LASIK, as it preserves the structural integrity of the anterior surface by requiring only a small incision, rather than cutting an entire flap. However, two main aspects should be considered that may explain the higher mechanical impact of SMILE in corneal tissue. To prevent lenticule rupture during extraction, 15 μm is added to the lenticule thickness. In addition, a 10% is added to the dioptric target to achieve the desired correction in clinical practice. These two aspects, combined with a 120 μm cap (which is thicker than the 100 μm flap used in LASIK) result in the removal of a quite significantly portion of corneal tissue, leaving a low percentage of RSB (see Table 8 for an example). SMILE is typically not performed for myopic corrections lower than 3 diopters due to the increased risk of lenticule rupture, making it unsuitable for correcting low refractive defects.

In the post-surgical scenario, the RSB is believed to bear the load exerted by the IOP and must therefore be preserved to prevent complications such as corneal ectasia. This assumption is supported by evidence that corneal stromal healing is minimal, with recovered strength reaching only 2.8% of that of a healthy cornea [37]. In our LASIK and SMILE simulations, we followed the same assumption by defining a frictionless contact at the interface between the flap/cap and the RSB in the post-surgical scenario, which we believe to be physiologically plausible.

PRK, the first procedure to enter clinical practice, has proven to be the least invasive treatment and is also the simplest, as corneal tissue is removed directly from the anterior surface, without the need to create a flap or extract a lenticule. However, the removal of the epithelium is necessary in this procedure, leading to significant post-surgical pain and discomfort. For this reason, LASIK is generally the preferred treatment by surgeons. From the mechanical perspective, it turned out to have an intermediate impact on corneal tissue.

Overall, the mechanical analysis revealed that, despite differences in mechanical impact among procedures, laser refractive surgeries induce low strains in corneal geometry (Fig. 8). Across all cases, the operating range remained within the toe region of the stress–strain curves (Fig. 4), an ECM-dominated, approximately isotropic regime. Consequently, even eyes with comparatively softer mechanics (R13, R14, R41, R51) achieved good optical outcomes despite their lower stiffness.

The study is not exempt from limitations. Epithelial remodeling could not be included, as patient-specific postoperative epithelial thickness maps and a validated remodeling law were not available. This may affect the predicted postoperative curvature and optical quality, particularly in eyes with more pronounced epithelial redistribution. Future studies should incorporate epithelial remodeling when longitudinal epithelial thickness data are available, enabling a more accurate prediction of postoperative optical outcomes.

Summarizing, a validation of a detailed methodology for refractive treatment simulations was presented, including the estimation of patient-specific material properties and IOP. This approach helped address a major limitation that has been prevalent in the literature, that is the lack of patient-specific material properties. A two-fold validation, not only of the methodology, but also of the tool for patient-specific IOP and material properties estimation, was presented. The proposed tool may offer a new perspective on refractive patient management by supporting clinicians in the pre-surgical decision-making process, providing both an optical prediction and a mechanical assessment of the treatment's impact on the patient. Within this context, the present work aligns with the emerging paradigm of *theramechanics*, in which biomechanical modeling is employed not only to interpret tissue behavior but also to support and optimize therapeutic interventions through mechanics-based personalization [38, 39]. Future work will extend the tool to account for patient-specific tissue response in the ablation depth calculation.

Appendix

A Alpins Method for Astigmatism Vector Analysis: Equations

To follow Alpins method for astigmatism vector analysis [36], astigmatism was represented in power-vector space using the Jackson cross-cylinder components J_0 and J_{45}, computed from cylinder magnitude C (in diopters) and axis α (in degrees, $\alpha \in [0, 180)$). Throughout, the axis convention was the *flat meridian* (as provided by Pentacam) and the same convention was applied to the FE outputs.

A.1 Cylinder/axis to Power Vectors

Given cylinder magnitude $C \geq 0$ and axis α, the power-vector components are

$$J_0 = -\frac{C}{2}\cos(2\alpha), \tag{A.1}$$

$$J_{45} = -\frac{C}{2}\sin(2\alpha), \tag{A.2}$$

where α is expressed in radians.

A.2 Power Vectors to Cylinder Magnitude and Axis

Given (J_0, J_{45}), the cylinder magnitude and axis are reconstructed as

$$|C| = 2\sqrt{J_0^2 + J_{45}^2}, \tag{A.3}$$

$$\alpha = \frac{1}{2}\,\mathrm{atan2}\big(J_{45},\, J_0\big). \tag{A.4}$$

A.3 Surgically Induced Astigmatism (SIA)

Let $(J_0^{\mathrm{pre}}, J_{45}^{\mathrm{pre}})$ and $(J_0^{\mathrm{post}}, J_{45}^{\mathrm{post}})$ be the pre- and postoperative power vectors, respectively. The SIA power-vector change is

$$\Delta J_0^{\mathrm{SIA}} = J_0^{\mathrm{post}} - J_0^{\mathrm{pre}}, \tag{A.5}$$

$$\Delta J_{45}^{\mathrm{SIA}} = J_{45}^{\mathrm{post}} - J_{45}^{\mathrm{pre}}. \tag{A.6}$$

The SIA magnitude and axis are obtained by applying Eqs. A.3–A.4 to $(\Delta J_0^{\mathrm{SIA}}, \Delta J_{45}^{\mathrm{SIA}})$:

$$|\mathrm{SIA}| = 2\sqrt{\big(\Delta J_0^{\mathrm{SIA}}\big)^2 + \big(\Delta J_{45}^{\mathrm{SIA}}\big)^2}. \tag{A.7}$$

A.4 Target-Induced Astigmatism (TIA)

TIA was derived from the intended astigmatic correction in the surgical treatment plan (manifest refraction cylinder and axis). The corresponding TIA power vectors are computed from Eqs. A.1–A.2:

$$J_0^{\mathrm{TIA}} = -\frac{C_{\mathrm{plan}}}{2}\cos\big(2\alpha_{\mathrm{plan}}\big), \tag{A.8}$$

$$J_{45}^{\mathrm{TIA}} = -\frac{C_{\mathrm{plan}}}{2}\sin\big(2\alpha_{\mathrm{plan}}\big), \tag{A.9}$$

and the TIA magnitude/axis follow from Eqs. A.3–A.4:

$$|\mathrm{TIA}| = 2\sqrt{\big(J_0^{\mathrm{TIA}}\big)^2 + \big(J_{45}^{\mathrm{TIA}}\big)^2}. \tag{A.10}$$

A.5 Difference Vector (DV)

The Difference Vector represents the residual astigmatic vector that would be required to change the achieved outcome into the intended outcome and is computed as the vector difference between TIA and SIA:

$$J_0^{\mathrm{DV}} = \Delta J_0^{\mathrm{TIA}} - J_0^{\mathrm{SIA}}, \tag{A.11}$$

$$J_{45}^{\mathrm{DV}} = \Delta J_{45}^{\mathrm{TIA}} - J_{45}^{\mathrm{SIA}}. \tag{A.12}$$

Its magnitude is

$$|\mathrm{DV}| = 2\sqrt{\big(J_0^{\mathrm{DV}}\big)^2 + \big(J_{45}^{\mathrm{DV}}\big)^2}. \tag{A.13}$$

A.6 Correction Index (CI)

In the Alpins method, the Correction Index (CI) is defined as the ratio of the magnitude of the surgically induced astigmatism to the magnitude of the target-induced astigmatism:

$$\mathrm{CI} = \frac{|\mathrm{SIA}|}{|\mathrm{TIA}|}. \tag{A.14}$$

CI = 1 indicates perfect correction in magnitude, CI > 1 indicates overcorrection in magnitude, and CI < 1 indicates undercorrection in magnitude.

B Patient-Specific Material Properties and Keratometry

(See Tables 9, 10 and 11).

Table 9 Patient-specific material properties and IOP

PRK					LASIK					SMILE				
PAT	C_{10} [kPa]	k_1 [kPa]	k_2 [-]	IOP [mmHg]	PAT	C_{10} [kPa]	k_1 [kPa]	k_2 [-]	IOP [mmHg]	PAT	C_{10} [kPa]	k_1 [kPa]	k_2 [-]	IOP [mmHg]
R01	47.80	129.54	997.86	12.96	R49	22.37	128.09	997.78	14.50	R21	63.52	92.63	967.70	10.16
R02	75.99	129.90	997.80	12.96	R50	28.76	129.30	997.87	10.82	R22	69.84	127.27	997.86	10.16
R03	51.30	129.90	991.64	9.53	R51	42.47	121.14	251.58	9.53	R27	36.33	129.28	997.35	9.53
R04	38.97	129.70	997.86	8.93	R52	51.35	129.80	997.86	10.16	R28	75.10	129.92	997.78	9.53
R05	22.70	125.38	997.61	9.53	R53	60.27	129.07	997.85	10.16	R29	50.07	129.49	996.54	10.16
R06	88.87	126.55	995.29	9.53	R54	91.33	114.08	943.99	9.53	R30	65.11	129.72	997.87	10.82
R07	42.88	128.03	997.44	10.16	R55	54.79	129.71	993.95	9.53	R31	98.99	125.99	883.96	10.82
R08	103.77	125.74	997.85	10.16	R56	40.54	129.92	992.26	9.53	R32	108.74	129.13	949.86	10.16
R09	85.28	127.87	997.53	10.82	R57	44.02	129.65	997.24	9.53	R33	33.47	126.42	997.33	8.93
R10	91.86	127.85	997.62	10.16	R58	88.20	129.87	997.80	8.93	R34	30.55	129.04	997.85	10.16
R11	44.09	114.21	872.91	10.82	R59	53.50	117.74	997.21	10.16	R35	78.07	129.21	983.81	10.16
R12	59.51	117.68	881.40	10.82	R60	71.43	115.76	997.86	10.82	R36	50.00	128.66	996.26	9.53
R13	78.00	116.04	344.52	10.16	R61	37.82	128.58	997.81	9.53	R37	30.12	129.47	997.86	9.53
R14	94.51	124.31	452.54	10.16	R62	103.21	128.73	997.83	10.16	R38	111.98	127.54	997.87	8.93
R15	31.40	124.45	989.11	9.53	R63	94.69	129.57	736.36	8.93	R39	15.67	114.79	997.74	11.51
R16	26.16	103.72	997.63	8.93	R64	44.33	129.88	997.83	9.53	R40	36.56	126.75	997.73	8.93
R17	14.91	120.50	997.87	9.53	R65	72.65	129.58	988.15	10.16	R41	36.17	126.25	226.38	8.93
R18	22.02	105.23	997.87	10.16	R66	107.61	129.66	994.25	10.16	R42	80.08	128.63	997.86	10.16
R19	59.00	128.54	990.00	10.16	R67	53.04	127.87	990.72	12.96					
R20	105.33	129.71	996.49	10.16	R68	24.95	123.78	997.85	16.11					

Table 10 Comparison of pre-surgical Pentacam and FE model refraction for PRK, LASIK, and SMILE patients

PRK								LASIK								SMILE							
	Pentacam			FE					Pentacam			FE					Pentacam			FE			
PAT	Km [D]	C [D]	axis [°]	Km [D]	C [D]	axis [°]	Err [D]	PAT	Km [D]	C [D]	axis [°]	Km [D]	C [D]	axis [°]	Err [D]	PAT	Km [D]	C [D]	axis [°]	Km [D]	C [D]	axis [°]	Err [D]
R01	42.8	1.0	12.2	43.0	1.1	12.0	0.2	R49	43.8	2.2	5.5	43.9	2.3	5.5	0.1	R21	42.4	0.7	3.9	42.5	0.8	4.0	0.1
R02	42.8	0.6	150.1	42.9	0.7	151.0	0.1	R50	44.1	2.2	179.3	44.2	2.3	179.0	0.1	R22	42.3	1.1	177.6	42.4	1.2	177.5	0.1
R03	43.5	1.5	2.4	43.6	1.6	2.0	0.1	R51	44.1	2.7	29.3	44.3	2.8	29.0	0.2	R27	42.6	1.0	9.6	42.8	1.0	9.7	0.2
R04	43.5	2.7	178.0	43.7	2.8	178.5	0.2	R52	44.1	2.6	158.0	44.2	2.7	158.5	0.1	R28	42.9	0.6	0.8	43.1	0.7	1.0	0.2
R05	44.1	0.2	168.5	44.1	0.3	169.7	0.0	R53	42.6	1.0	145.9	42.9	1.0	144.9	0.3	R29	42.9	0.6	4.6	43.0	0.7	4.5	0.1
R06	44.1	0.4	0.2	44.1	0.5	175.9	0.0	R54	42.5	0.9	43.4	42.4	1.1	45.3	−0.1	R30	42.6	0.6	174.7	42.7	0.7	175.0	0.1
R07	43.2	0.8	92.3	43.3	0.9	92.0	0.1	R55	43.0	0.7	8.5	43.1	0.8	8.5	0.1	R31	43.0	0.7	157.7	43.0	0.7	158.9	0.0
R08	44.0	1.0	61.7	44.1	1.1	62.0	0.1	R56	43.0	0.7	175.2	43.1	0.8	175.0	0.1	R32	43.0	0.7	4.5	43.0	1.5	1.0	0.0
R09	43.0	1.0	167.5	43.2	1.1	167.1	0.2	R57	43.5	0.9	5.7	43.8	1.1	5.0	0.3	R33	45.1	1.3	172.5	45.2	1.4	172.0	0.1
R10	43.3	1.3	16.2	43.5	1.5	16.0	0.2	R58	43.0	0.7	174.5	43.0	0.9	175.9	0.0	R34	45.1	1.5	4.6	45.2	1.6	5.0	0.1
R11	45.1	1.1	1.3	45.2	1.2	1.0	0.1	R59	42.2	0.5	149.0	42.3	0.6	149.0	0.1	R35	43.0	0.8	175.5	43.2	0.9	175.5	0.2
R12	45.1	1.2	176.9	45.2	1.3	177.5	0.1	R60	42.3	0.4	160.0	42.4	0.5	160.0	0.1	R36	42.9	0.9	178.4	42.8	0.9	177.2	−0.1
R13	43.8	1.1	170.9	44.0	1.1	172.5	0.2	R61	43.7	1.1	1.8	43.8	0.9	2.3	0.1	R37	42.8	0.8	5.6	42.7	0.9	5.4	−0.1
R14	43.5	0.7	171.1	43.6	0.7	177.9	0.1	R62	43.5	0.8	176.3	43.5	0.5	0.5	0.0	R38	42.9	1.0	174.4	42.8	0.9	174.5	−0.1
R15	43.1	0.6	171.3	43.2	0.7	171.0	0.1	R63	43.9	1.0	170.0	44.0	1.1	170.0	0.1	R39	46.9	0.9	23.3	47.0	1.0	23.5	0.1
R16	43.8	0.6	7.2	43.9	0.7	7.0	0.1	R64	43.9	1.5	2.6	44.0	1.6	3.0	0.1	R40	46.8	0.9	152.1	46.9	1.0	152.0	0.1
R17	45.6	1.2	32.0	45.7	1.3	32.5	0.1	R65	43.9	1.5	5.6	44.1	1.4	6.6	0.2	R41	45.4	0.4	132.1	45.5	0.5	132.0	0.1
R18	45.4	0.5	104.7	45.5	0.6	105.0	0.1	R66	43.7	2.0	174.6	44.2	2.4	173.1	0.5	R42	45.6	0.2	64.3	45.7	0.3	64.5	0.1
R19	43.2	0.3	125.4	43.2	0.3	104.2	0.0	R67	43.4	1.6	179.2	43.5	1.7	179.0	0.1								
R20	42.9	0.2	120.1	42.9	0.3	117.9	0.0	R68	43.5	1.2	176.7	43.6	1.3	177.0	0.1								

Km = mean keratometry; C = cylinder; axis = astigmatism axis; $Err = Km(FE) - Km(PENTACAM)$

Table 11 Comparison of post-surgical Pentacam and FE model refraction for PRK, LASIK, and SMILE patients. Km = mean keratometry; C = cylinder; axis = astigmatism axis; $Err = Km(FE) - Km(PENTACAM)$

PRK								LASIK								SMILE							
	Pentacam			FE					Pentacam			FE					Pentacam			FE			
PAT	Km [D]	C [D]	axis [°]	Km [D]	C [D]	axis [°]	Err [D]	PAT	Km [D]	C [D]	axis [°]	Km [D]	C [D]	axis [°]	Err [D]	PAT	Km [D]	C [D]	axis [°]	Km [D]	C [D]	axis [°]	Err [D]
R01	41.0	0.2	160.6	41.5	0.3	161.0	0.5	R49	41.6	1.0	153.3	42.0	1.1	153.5	0.4	R21	40.2	0.8	178.5	40.3	0.9	178.6	0.1
R02	40.8	0.7	25.7	41.1	0.8	26.0	0.3	R50	42.0	0.9	156.1	42.3	1.0	156.0	0.3	R22	40.3	1.0	178.5	40.5	1.1	178.4	0.2
R03	41.7	1.4	39.5	42.0	1.5	39.0	0.3	R51	41.5	0.4	125.4	41.7	0.5	125.0	0.2	R27	40.2	1.1	16.3	40.8	1.1	14.7	0.6
R04	41.4	0.8	164.9	41.6	0.9	165.0	0.2	R52	41.6	0.4	44.5	41.8	0.5	44.7	0.2	R28	40.6	1.1	173.0	41.4	0.8	172.3	0.8
R05	42.0	0.7	169.9	42.4	0.4	170.0	0.4	R53	40.2	0.3	20.9	41.0	1.0	33.4	0.8	R29	40.0	0.2	25.6	40.3	0.3	25.5	0.3
R06	41.9	0.6	5.4	42.5	0.5	177.6	0.6	R54	39.5	0.6	157.4	39.9	0.7	137.2	0.4	R30	40.0	0.4	0.9	40.2	0.5	1.1	0.2
R07	41.2	0.2	21.7	41.4	0.3	22.0	0.2	R55	40.9	1.0	5.6	41.1	1.1	5.8	0.2	R31	40.2	0.3	134.1	40.6	0.5	174.2	0.4
R08	41.7	0.5	175.3	42.0	0.6	175.5	0.3	R56	40.8	1.0	170.2	41.1	1.1	170.5	0.3	R32	40.3	0.3	40.2	40.8	1.5	178.5	0.5
R09	40.0	0.8	162.4	40.9	1.1	167.3	0.9	R57	40.1	0.1	165.1	40.5	1.1	9.6	0.4	R33	42.3	1.3	178.8	42.6	1.4	179.0	0.3
R10	40.5	0.9	175.8	40.9	1.5	13.5	0.4	R58	40.2	0.5	160.5	40.6	0.9	167.6	0.4	R34	42.2	1.6	4.9	42.3	1.7	5.0	0.1
R11	41.3	0.4	178.1	41.8	0.5	178.5	0.5	R59	39.3	0.5	37.3	39.4	0.6	37.5	0.1	R35	38.9	0.7	171.6	40.1	0.9	176.8	1.2
R12	41.0	0.3	157.6	41.4	0.4	158.0	0.4	R60	40.1	0.9	81.1	40.3	1.0	81.3	0.2	R36	39.1	0.8	3.2	39.0	0.9	1.3	−0.1
R13	39.6	1.0	173.3	40.6	1.1	173.3	1.0	R61	41.8	0.5	11.6	41.8	1.0	2.2	0.0	R37	38.4	0.3	162.6	38.8	0.9	174.6	0.4
R14	39.6	1.0	173.3	39.9	0.8	165.0	0.3	R62	39.4	0.8	14.9	40.3	0.9	24.4	0.9	R38	38.7	0.5	9.4	39.3	1.0	6.5	0.6
R15	38.7	1.3	177.5	38.9	1.4	177.0	0.2	R63	40.0	0.7	8.4	40.4	0.8	8.6	0.4	R39	43.4	1.0	6.3	43.8	1.1	6.5	0.4
R16	39.6	1.1	10.9	39.9	1.2	11.0	0.3	R64	39.6	0.4	178.5	39.8	0.5	178.4	0.2	R40	43.4	1.2	162.8	43.9	1.3	163.0	0.5
R17	39.3	1.3	5.6	39.3	1.4	6.0	0.0	R65	39.0	1.0	4.4	40.1	1.4	5.2	1.1	R41	40.5	0.3	164.5	40.8	0.4	164.7	0.3
R18	41.5	0.5	3.6	41.6	0.6	4.0	0.1	R66	38.9	0.7	10.5	40.2	2.3	177.8	1.3	R42	40.5	0.0	113.5	40.9	0.1	113.8	0.4
R19	39.5	0.8	3.0	39.3	0.3	99.9	−0.2	R67	38.6	0.4	39.6	39.1	0.5	39.8	0.5								
R20	39.3	0.8	158.3	39.3	0.3	118.3	0.0	R68	38.6	0.8	164.3	38.9	0.9	164.5	0.3								

Funding Open Access funding provided thanks to the CRUE-CSIC agreement with Springer Nature. This work received funding from the University of Zaragoza (project I-2021/010/PIP OBERON – Opto-Biomechanical Eye Research Network/PIP); from the Spanish Ministerio de Ciencia, Innovación y Universidades through grant PID2023-147987OB-C31, financed by MICIU/AEI/10.13039/501100011033 and by FEDER, EU; and from the Government of Aragon through research group grant T24-20R (co-financed by FEDER). Part of the work was performed at the ICTS "NANBIOSIS," specifically the High Performance Computing Unit (U27) of CIBER in Bioengineering, Biomaterials & Nanomedicine (CIBER-BBN) at the University of Zaragoza. CIBER activities are financed by the Instituto de Salud Carlos III with assistance from the European Regional Development Fund.

Declarations

Conflict of interest The authors have no relevant financial or non-financial interests to disclose.

References

1. Francis, M., R. Shetty, P. Padmanabhan, R. Vinciguerra, P. Vinciguerra, M. Lippera, et al. New simulation software to predict postoperative corneal stiffness before laser vision correction. *Journal of Cataract & Refractive Surgery.* 49(6):620–627, 2023. https://doi.org/10.1097/j.jcrs.0000000000001169.
2. Im Kim, T., J. L. A. del Barrio, M. Wilkins, B. Cochener, and M. Ang. Refractive surgery. *The Lancet.* 393:2085–2098, 2019. https://doi.org/10.1016/S0140-6736(18)33209-4.
3. Moshirfar, M., M. N. Motlagh, M. S. Murri, H. Momeni-Moghaddam, Y. C. Ronquillo, and P. C. Hoopes. Advances in Biomechanical Parameters for Screening of Refractive Surgery Candidates: A Review of the Literature, Part III. *Medical Hypothesis, Discovery & Innovation in Ophthalmology.* 8(3):219–240, 2019.
4. Sandoval, H. P., E. D. Donnenfeld, T. Kohnen, R. L. Lindstrom, R. Potvin, D. M. Tremblay, et al. Modern laser in situ keratomileusis outcomes. *Journal of Cataract and Refractive Surgery.* 42:1224–1234, 2016. https://doi.org/10.1016/j.jcrs.2016.07.012.
5. Sánchez, P., K. Moutsouris, and A. Pandolfi. Biomechanical and optical behavior of human corneas before and after photorefractive keratectomy. *Journal of Cataract and Refractive Surgery.* 40:905–917, 2014. https://doi.org/10.1016/j.jcrs.2014.03.020.
6. Simonini, I., and A. Pandolfi. Customized finite element modelling of the human cornea. *PLoS ONE.* 10:1–23, 2015. https://doi.org/10.1371/journal.pone.0130426.
7. Dupps, W. J. J., and I. Seven. A Large-Scale Computational Analysis of Corneal Structural Response and Ectasia Risk in Myopic Laser Refractive Surgery. *Transactions of the American Ophthalmological Society.* 114:T1, 2016.
8. Seven, I., A. Vahdati, V. S. D. Stefano, R. R. Krueger, and W. J. Dupps. Comparison of patient-specific computational modeling predictions and clinical outcomes of lasik for myopia. *Investigative Ophthalmology and Visual Science.* 57:6287–6297, 2016. https://doi.org/10.1167/iovs.16-19948.
9. Bao, F. J., J. J. Wang, S. Cao, N. Liao, B. Shu, Y. P. Zhao, et al. Development and clinical verification of numerical simulation for laser in situ keratomileusis. *Journal of the Mechanical Behavior of Biomedical Materials.* 83:126–134, 2018. https://doi.org/10.1016/j.jmbbm.2018.04.016.
10. Seven I, Lloyd JS, Dupps WJ. Differences in simulated refractive outcomes of photorefractive keratectomy (PRK) and laser in-situ keratomileusis (LASIK) for myopia in same-eye virtual trials. International Journal of Environmental Research and Public Health. 2020;17. https://doi.org/10.3390/ijerph17010287.
11. Fang, L., W. Ma, Y. Wang, Y. Dai, and Z. Fang. Theoretical analysis of wave-front aberrations induced from conventional laser refractive surgery in a biomechanical finite element model. *Investigative Ophthalmology and Visual Science.* 61:1–11, 2020. https://doi.org/10.1167/IOVS.61.5.34.
12. Katzengold, R., A. Gefen, N. Sorkin, D. Smadja, and D. Varssano. Simulation of the biomechanical effects induced by laser in situ keratomileusis (LASIK) for different levels of ablation in normal corneas. *Eye (Basingstoke).* 35:996–1001, 2021. https://doi.org/10.1038/s41433-020-1017-7.
13. Fantaci, B., B. Calvo, R. Barraquer, A. Picó, and Ariza-Gracia M. Ángel. Establishing Standardization Guidelines For Finite-Element Optomechanical Simulations of Refractive Laser Surgeries: An Application to Photorefractive Keratectomy. *Translational Vision Science & Technology.* 13:11, 2024. https://doi.org/10.1167/tvst.13.5.11.
14. Fantaci, B., J. F. Rodriguez Matas, V. Squartecchia, L. Vavassori, and B. Calvo. Unraveling the Impact of Laser Refractive Surgery on Corneal Ectasia: An In Silico Study. *Frontiers in Bioengineering and Biotechnology.* 13:1548539, 2025. https://doi.org/10.3389/fbioe.2025.1548539.
15. Montanino A, van Overbeeke S, Pandolfi A. Modelling the biomechanics of laser corneal refractive surgery. Journal of the Mechanical Behavior of Biomedical Materials. 2023;p. 105998. https://doi.org/10.1016/j.jmbbm.2023.105998.
16. Luo, S., X. Li, Y. Fan, L. He, G. Luo, F. Bao, et al. Differences in the Corneal Biomechanical Responses to LASIK and KLEx Based on Parametric Numerical Simulation. *Journal of Refractive Surgery.* 41(9):e975–e989, 2025. https://doi.org/10.3928/1081597X-20250707-06.
17. Büchler, P., M. H. Nambiar, M. Frigelli, A. Sinha Roy, T. G. Seiler, and M. Á. Ariza-Gracia. Biomechanical Comparison of PRK, LASIK, and KLEx Using Personalized Finite Element Simulations. *Journal of Refractive Surgery.* 41(10):e1138–e1148, 2025. https://doi.org/10.3928/1081597X-20250806-01.
18. Moin, K. A., and M. Moshirfar. A Toolkit for Patients Evaluating Benefits and Risks of LASIK. *Expert Review of Ophthalmology.* 19(6):405–408, 2024. https://doi.org/10.1080/17469899.2024.2394214.
19. dell'Isola, F., F. D'Annibale, R. Luciano, T. Henze, and I. Giorgio. A generalised plate with kinematically independent thickness for modelling shapes of corneas affected by keratoconus before and after penetrating keratoplasty. *Mathematics and Mechanics of Solids.* :1–15, 2025. https://doi.org/10.1177/10812865251345814.
20. Nagle, M., H. Conroy Broderick, A. Buganza Tepole, M. Fop, and Annaidh A. Ní. A machine learning approach to predict in vivo skin growth. *Scientific Reports.* 14(1):17456, 2024. https://doi.org/10.1038/s41598-024-67056-z.

21. Ahmadi, M., D. Biswas, R. Paul, M. Lin, Y. Tang, T. S. Cheema, et al. Integrating finite element analysis and physics-informed neural networks for biomechanical modeling of the human lumbar spine. *North American Spine Society Journal.*17(22):100598, 2025. https://doi.org/10.1016/j.xnsj.2025.100598.
22. Redaelli, E., B. Calvo, J. F. Rodriguez Matas, G. Luraghi, and J. Grasa. A POD-NN methodology to determine in vivo mechanical properties of soft tissues. Application to human cornea deformed by Corvis ST test. *Computers in Biology and Medicine*. 187:109792, 2025. https://doi.org/10.1016/j.compbiomed.2025.109792.
23. Redaelli, E., J. Grasa, B. Calvo, J. F. R. Matas, and G. Luraghi. A detailed methodology to model the Non Contact Tonometry: a Fluid Structure Interaction study. *Frontiers in Bioengineering and Biotechnology.* 10:1–12, 2022. https://doi.org/10.3389/fbioe.2022.981665.
24. McNabb, R. P., S. Farsiu, S. S. Stinnett, J. A. Izatt, and A. N. Kuo. Optical coherence tomography accurately measures corneal power change from laser refractive surgery. *Ophthalmology.* 122(4):677–686, 2015. https://doi.org/10.1016/j.ophtha.2014.10.003.
25. Redaelli E, Calvo B, Rodriguez Matas JF, Luraghi G, Grasa J. Non-contact tonometry: predicting intraocular pressure using a material-corneal thickness-independent methodology. Frontiers in Bioengineering and Biotechnology. 2024;12:1406870. Published on July 25, 2024. https://doi.org/10.3389/fbioe.2024.1406870.
26. Holzapfel, G. A., T. C. Gasser, and R. W. Ogden. A new constitutive framework for arterial wall mechanics and a comparative study of material models. *Journal of elasticity and the physical science of solids.* 61:1–48, 2000.
27. Pandolfi, A., G. Fotia, and F. Manganiello. Finite element simulations of laser refractive corneal surgery. *Engineering with Computers.* 25:15–24, 2009. https://doi.org/10.1007/s00366-008-0102-5.
28. Simonini I, Annaidh AN, Pandolfi A. Numerical estimation of stress and refractive power maps in healthy and keratoconus eyes. Journal of the Mechanical Behavior of Biomedical Materials. 2022;131. https://doi.org/10.1016/j.jmbbm.2022.105252.
29. Ariza-Gracia, M., J. Zurita, D. P. Piñero, B. Calvo, and J. F. Rodríguez-Matas. Automatized Patient-Specific Methodology for Numerical Determination of Biomechanical Corneal Response. *Annals of Biomedical Engineering.* 44:1753–1772, 2016. https://doi.org/10.1007/s10439-015-1426-0.
30. Mröchen, M., C. Donitzky, C. Wullner, and J. Loffler. Wavefront-optimized ablation profiles: Theoretical background. *Journal of Cataract and Refractive Surgery.* 30:775–785, 2004. https://doi.org/10.1016/j.jcrs.2004.01.026.
31. Wang C, Li X, Guo Y, He R, Guo H, Chen W. Effects of Laser In Situ Keratomileusis and Small-Incision Lenticule Extraction on Corneal Biomechanical Behavior: A Finite Element Analysis. Frontiers in Bioengineering and Biotechnology. 2022;10. https://doi.org/10.3389/fbioe.2022.855367.
32. Blanco-Martínez, I., J. M. González-Méijome, and M. Faria-Ribeiro. Linear fitting of biconic surfaces for corneal modeling. *Journal of the Optical Society of America.* 41:288, 2024. https://doi.org/10.1364/josaa.505248.
33. Cavas-Martínez, F., E. D. la Cruz Sánchez, J. N. Martínez, F. J. F. Cañavate, and D. G. Fernández-Pacheco. Corneal topography in keratoconus: state of the art. *Eye and Vision.* 3:1–12, 2016. https://doi.org/10.1186/s40662-016-0036-8.
34. Kanellopoulos AJ.: Corneal Topography/Tomography Explained. Accessed: 2024–11-04.
35. Schwiegerling, J., and R. W. Snyder. Custom Photorefractive Keratectomy Ablations for the Correction of Spherical and Cylindrical Refractive Error and Higher-Order Aberration. *Journal of the Optical Society of America A: Optics, Image Science, and Vision.* 15(9):2572–2579, 1998. https://doi.org/10.1364/josaa.15.002572.
36. Alpins, N. Astigmatism analysis by the Alpins method. *Journal of Cataract and Refractive Surgery.* 27(1):31–49, 2001. https://doi.org/10.1016/S0886-3350(00)00798-7.
37. Schmack, I., D. G. Dawson, B. E. McCarey, G. O. R. Waring, H. E. Grossniklaus, and H. F. Edelhauser. Cohesive tensile strength of human LASIK wounds with histologic, ultrastructural, and clinical correlations. *Journal of Refractive Surgery.* 21(5):433–445, 2005. https://doi.org/10.3928/1081-597X-20050901-04.
38. Allena, R., and Y. Rémond. Theramechanics: How Acting on Mechanics Will Help Conceive New Medical Treatments. *Mathematics and Mechanics of Complex Systems.* 11(4):541–566, 2023. https://doi.org/10.2140/memocs.2023.11.541.
39. Allena, R., and Y. Rémond. How Can Theramechanics Drive Bone Remodeling? *Mathematics and Mechanics of Complex Systems.* 13(1):55–71, 2025. https://doi.org/10.2140/memocs.2025.13.55.